Modeling Proton Exchange Membrane Fuel Cells—A Review

Ayodeji Demuren and Russell L. Edwards

1 Introduction

This paper is written in commemoration of D. Brian Spalding (DBS), who made significant contributions to the theory and practice of combustion. He wrote his Ph.D. thesis on the combustion of liquid fuels in 1951 [1], followed by several papers in this field [2, 3] and culminating in a couple of textbooks. A general theory on turbulent combustion [4] and combustion and mass transfer [5]. Combustion relies on thermochemical processes to derive energy from burning fuels. This invariably occurs at high temperatures, and the thermodynamic efficiency is limited by the Carnot cycle. On the other hand, fuel cells are electrochemical devices which convert energy from simple fuel and oxidant chemical reactions, at the anode and the cathode, directly into electrical energy. These can occur over a wide range of temperatures, and the thermodynamic efficiency is not limited by the Carnot cycle, and so are expected to deliver energy from the fuels more efficiently, due to the direct nature of the process. An excellent treatise on fuel cells by Dicks and Rand [6] shows that this is mostly true, especially at lower temperatures. In effect, fuel cells are like continuous batteries, which can operate endlessly as long as the electrodes are supplied with fuel and oxidant, respectively, and the conditions for the chemical reactions are maintained. In contrast to secondary (rechargeable) batteries, neither the electrodes nor the electrolyte is consumed, so no recharging is necessary. In the early days of the automobile [7], battery-powered electric vehicles were in competition with those powered by internal combustion engines (ICE): a competition that was won easily by the latter, because of their reliability and range. Fuel cells have the potential to increase the range of electric vehicles, thereby making them viable again. But recent improvements in the technology of secondary batteries have greatly expanded options for battery-powered electric vehicles. There are many different types of fuel

A. Demuren (✉) · R. L. Edwards
Department of Mechanical and Aerospace Engineering,
Old Dominion University, Norfolk, VA, USA
e-mail: ademuren@odu.edu

A. Runchal (ed.), *50 Years of CFD in Engineering Sciences*,
https://doi.org/10.1007/978-981-15-2670-1_15

cells and technology implementations, which are reviewed in the excellent treatise [6]. The most common of these is the polymer electrolyte membrane or proton exchange membrane fuel cells (PEMFC), which use thin layers of polymer-based solid electrolyte, along with catalyst infused conductive electrodes. They are the basis of the so-called Hydrogen economy.

PEMFC are electrochemical energy conversion devices that produce electrical energy from the chemical energy present in hydrogen fuel when it reacts with oxygen in a cell. Water and fractional waste heat are the byproducts. Because of the low operational temperature, typically 25–80 °C, PEMFC has been used in automotive, marine, and portable electronics applications where they produce useful electrical energy at high efficiency, without creating the pollutants associated with combustion of fossil fuels. They exhibit high efficiency in the range of 60% when used for electrical energy conversion and 80% when there is cogeneration of electrical and thermal energy. The main hindrances to wider adoption have been high cost, low lifespan, and wider availability of hydrogen fuel. The suitability of PEM fuel cells for particular applications is determined in terms of power density, cost per kilowatt, and durability (a lifetime of operation in hours). Each cell can only produce a fraction of a volt, during operation, so systems have to be built with stacks of cells, in series, to obtain useable voltage. Depending on application, systems have been created with power of only a few Watts to hundreds of Kilowatts. At the low end are devices for powering mobile electronics, and at the high end are powertrains for public transportation such as electric busses. Durability goals also vary based on application, which could be a few thousand operating hours in transportation use, to hundreds of thousands of hours in stationary power generation use. Material degradation of key components typically limits durability. Performance degrades gradually over time. The choice of cell design and operating conditions will typically influence some vectors of performance degradation, such as membrane degradation, or the reduction of effective catalyst surface area with agglomeration or aging.

Water and thermal management are fundamentally intertwined problems which will influence the durability, performance, and efficiency of a PEM fuel cell. The reactant gases are commonly highly humidified even though the device produces water in operation. The humidification is done to ensure high protonic conductivity and efficiency from the water-absorbing (PEM) membrane at the heart of the fuel cell.

Complexity of fuel cell design, along with the thinness of several of the membranes involved make experimental measurements extremely difficult. Hence, computational fluid dynamics (CFD) approach is widely used for PEMFC design and simulation [8]. These mostly follow the computational techniques developed at Imperial College under the supervision of DBS. Early pioneering computational modeling effort was isothermal and only one-dimensional. It was helpful in establishing the fundamental models and relationships, but is generally thought to be inadequate in analyzing three-dimensional flow effects that interact with electrochemical reactions of the PEMFC. Later models account for three-dimensional effects that many analytical solutions will neglect or not consider. This approach has been implemented successfully in many commercial CFD codes, however, computational costs remain

quite high. The PEMFC is a multiscale problem. Costs are driven by the requirements to mesh/discretize the flow channels (~mm thickness), simultaneously with the extremely thin catalyst and electrolyte layers, the membrane electrode assembly (MEA), that are two to three orders of magnitude thinner.

Another approach is to omit the thin MEA from the computational domain, treating the MEA as an interface, between the anode and cathode flow domains. The MEA can be treated as a reacting wall, with consumption/production source terms on either side to mimic its operation. The interface model [9, 10] then matches these effects as boundary conditions to both domains. Models considering similar state, dimensionality, and effects (physics) will then differ, primarily, in how they treat the MEA [11]. The physics of the MEA include water transport, heat transport, gaseous diffusion, and the kinetics of the reactions occurring in the anode and cathode. A multitude of subsequent studies have improved the understanding of each area from the time when CFD models were first being developed and refined [12] Some widely used modeling assumptions have been called into question by direct experimental evidence [13]. Many analytical approaches to model catalyst layer operation have also been published.

2 PEM Fuel Cell Fundamentals

The PEMFC is an electrochemical energy conversion device that converts the internal chemical energy of the reactants (the hydrogen fuel and the oxygen oxidizer), into electrical energy. The basic components of the PEMFC are shown in a cutaway diagram in Fig. 1. The left side is the negative, or anode terminal, and the right side the positive, or cathode terminal. Electrical connection to an external circuit is made via the electrically conductive current collector plates. Both current collector plates typically have gas flow channels that direct the flow of the hydrogen fuel to the anode side, and the oxygen or air oxidizer to the cathode side. The fuel and oxidizer, collectively referred to as reactants, are typically supplied in carefully metered amounts as pressurized, humidified gas streams.

At the anode, hydrogen is oxidized in the hydrogen oxidation reaction (HOR) into its constituent protons (H^+) and electrons (e^-). The HOR occurs at reaction sites (catalyst particles) distributed through the thickness of the anode catalyst layer (ACL) where diatomic hydrogen is split into two protons and two electrons:

$$H_2 \rightarrow 2H^+ + 2e^- \tag{1}$$

The protons produced by this reaction move through the thickness of the solid electrolyte membrane to reach the cathode catalyst layer (CCL) under the influence of the electric field. Electrons reach the CCL through the external circuit, and oxygen gas reaches the CCL by diffusing through the diffusion media. At reaction sites, distributed through the thickness of the CCL, the oxygen reduction reaction (ORR) combines oxygen, protons, and electrons, creating water as the reaction product:

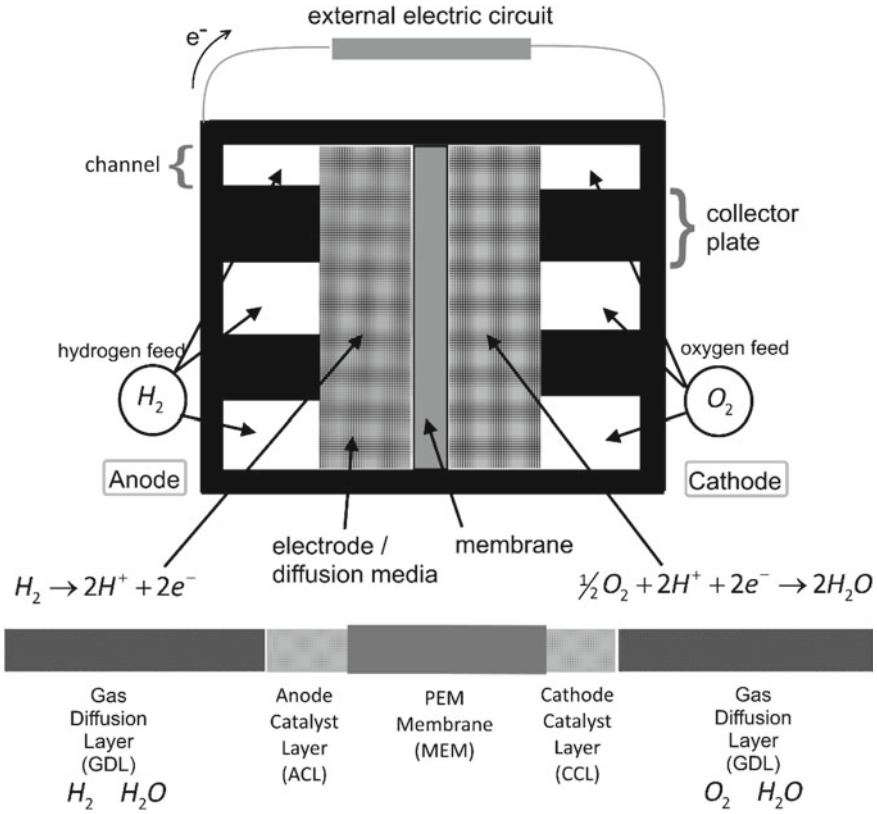

Fig. 1 Schematic slice of a single cell PEMFC

$$O_2 + 4H^+ + 4e^- \rightarrow 2H_2O \tag{2}$$

The product water hydrates the membrane, and will leave the cell through the reactant gas streams. Water movement within the membrane depends on operating conditions. Both anode and cathode gas streams exchange water with the MEA, and remove product water from the device.

Collector plates serve both as the electric terminals of the cell, in which role they collect electrons generated at the catalyst layers, as well as flow channels to distribute the humidified gases over the surface of the anode and cathode. Collector plates have been made from graphite and various metals to have the desired electrical conductivity and resistance to corrosion.

Gas diffusion layers (GDL) contact both sides of the MEA. These provide electronic and heat conduction between the collector plates and the MEA. They are highly porous in order to allow the gases in the flow channels to diffuse through to the MEA. The diffusion media typically is made of carbon cloth or carbon paper materials, with thicknesses ~150–400 μm typical.

Catalyst layers are attached to both the anode (ACL) and cathode (CCL) sides of the central polymer electrolyte membrane (PEM). These are porous structures consisting of three phases. Fine catalyst particles of platinum (Pt) or an alloy thereof provide the reaction sites distributed throughout the CL thickness. These are supported on complex structures of carbon particles that provide electronic conduction within the catalyst layers. This carbon-supported platinum catalyst (often denoted as PT/C) technology creates a large number of active catalyst sites and a catalytic surface area several orders of magnitude greater than the planar electrode surface area, so that the reaction can proceed at a feasible rate. A dispersed electrolyte phase serves, likewise, to allow protonic conduction to the reaction sites. The remainder void volume consists of pores to allow for gas permeation. Typical thicknesses are 5–15 μm.

The electrolyte membrane serves to separate the two respective gas flows. The membrane must, according to its function, be highly conductive of the protons while simultaneously nonconductive for electrons in order to avoid short-circuiting the external flow of electricity. Nafion has been the common electrolyte material. It absorbs water, possibly 40% or more by weight, when in contact with humidified gases, and when so hydrated, becomes proton-conductive. Protonic conductivity rises significantly with water content, allowing the device to operate efficiently. Typical electrolyte membrane thicknesses range from (25 μm) to (175 μm). Thinner membranes have been more popular for some time.

Coupled chemical reactions occur on opposite sides of the planar catalyzed membrane. Convective and diffusive transport of reactant gases occur within separated flow channels on both the anode and cathode sides. Each gas permeates through a gas diffusion layer (GDL) and reaches the respective anode and cathode catalyst layers where corresponding electrochemical reactions occur. Continuous operation requires conduction of protons through the central membrane MEA, as well as conduction of electrons through the GDL, graphite flow field plates, and an external electrical circuit.

The overall chemical reaction can be written, combining Eqs. (1) and (2), as

$$H_2 + \frac{1}{2}O_2 \rightarrow H_2O \tag{3}$$

The performance, or device efficiency, of a PEM fuel cell is typically assessed through a voltage measurement conducted over a range of current densities, known as a polarization curve or characteristic curve. The curve is typically analyzed by computing an ideal, thermodynamic voltage, and then subtracting estimates of various polarizations (losses) from it. Under ideal conditions, the maximum thermodynamic work that can be done in the reversible reaction, at constant pressure and temperature, is the change in Gibb's free energy of the products and reactants. For the reaction of Eq. (3), 1 mol of hydrogen reacts with half a mol of oxygen to produce 1 mol of water. In the process two mols of electrons are exchanged through the external circuit. The corresponding change in Gibb's free energy is

$$\Delta g_f = \left\{ (\Delta g_f)_{H_2O} - [(\Delta g_f)_{H_2} + \frac{1}{2}(\Delta g_f)_{O_2}] \right\} \tag{4}$$

For liquid water product at 80 °C, $\Delta g_f = -228.2 \frac{\text{KJ}}{\text{mol}}$

The corresponding charge is $-2F$, where F, the Faraday number, is the charge of 1 mol of electrons.

Hence, the electrical work done, (current × voltage) is $-2FV$.

Therefore, if the process is reversible, with no losses, the reversible, or maximum open-circuit voltage (OCV) is

$$V_r = \frac{\Delta g_f}{-2F} = \frac{-228{,}200}{-2 * 96{,}485} = 1.18\,\text{V} \tag{5}$$

Once current is drawn from the cell, there will be losses and the process is no longer reversible, and the cell voltage will be reduced. The polarization curve, (Fig. 2) shows how the cell voltage decreases with current density [14]. These losses are associated with decreased efficiency in the conversion of the chemical energy to electrical energy in the PEMFC. The maximum efficiency, based on the higher heating value (HHR), $\Delta h_f = -285.84 \frac{\text{KJ}}{\text{mol}}$, in which the reaction product is liquid, is 80%, compared to typical operational efficiency of 60%.

It is noted that the maximum efficiency decreases slightly with temperature, whereas that of a heat engine, limited by the Carnot cycle increases with temperature, with a crossover point around 1000 K [14]. Therefore, fuel cells which operate at high temperatures, such as the Solid Oxide Fuel Cell (SOFC) may have lower nominal efficiency than a comparable heat engine.

The *Nernst equation* can be used to calculate changes in OCV, based on concentration or partial pressures of reactants and products, as

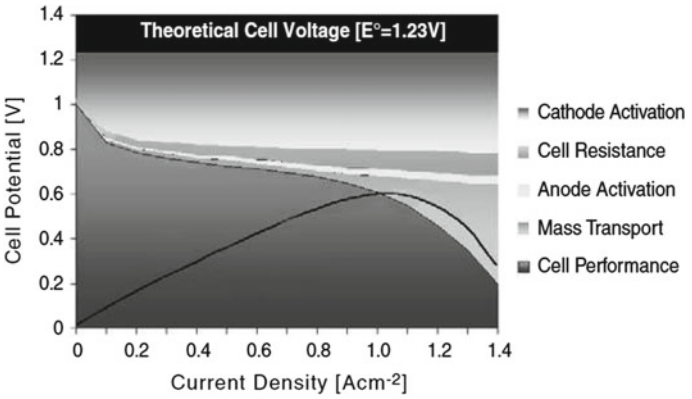

Fig. 2 Polarization curve showing sources of performance losses in a PEMFC operating at 25 °C. Power curve is also shown [14]

$$V_r = V_r^o + \frac{RT}{2F} \ln\left(\frac{P_{H_2} \cdot P_{O_2}^{1/2}}{P_{H_2O}}\right) \tag{6}$$

where V_r^o is the OCV at standard pressure, R is the universal gas constant, T is the absolute temperature, and the P's are the respective partial pressures. Therefore, higher stoichiometric values of reactants would produce higher OCV. Also the use of pure oxygen at the cathode instead of air.

Performance losses within the PEMFC can be categorized based on different mechanisms. The major categories of losses within the cell are activation (or kinetic), ohmic, and mass transport (or concentration) polarizations.

Activation losses describe the voltage drop required to drive both the anode and cathode chemical reactions at rates greater than equilibrium. Also known as activation polarization, kinetic losses tend to dominate the voltage drop occurring in the PEMFC at low-current densities. As shown in Fig. 2, activation losses occurring from the ORR at the CCL tend to be more significant than those in the ACL. These losses are described by models of electrochemical kinetics, and are greatly influenced by catalyst site temperature, gas composition, and the effective catalyst site surface area, which is itself dependent upon the complex catalyst layer roughness and composition. The *Tafel equation* can be used to calculate the activation losses in terms of exchange current density as

$$\Delta V_{\text{act}} = \frac{RT}{2\alpha F} \ln\left(\frac{i}{i_o}\right) \tag{7}$$

where i_o is the exchange current density, and α is the charge transfer coefficient with a typical value between 0.1 and 0.5. The higher the value of i_o, the more active is the electrode and the smaller the activation voltage loss. This equation represents the limiting behavior of the Butler–Volmer equations, to be discussed in a later section.

Ohmic losses within the PEMFC are 'iR' type losses. These tend to dominate the voltage drop occurring in the PEMFC at mid-range current densities. Thus the measured voltage curve decreases almost linearly with current density. Relatively minor ohmic losses come from electronic conduction losses within PEMFC components and contact resistances. Primary measurable ohmic losses come from the ionic resistance of the membrane, which is dependent upon its state of hydration and temperature. The use of thin membranes helps to minimize ohmic losses.

Mass transport, or concentration, losses occur under high current density operation. These arise from the inability to replenish the supply of reactants at the reaction sites fast enough. When reactant consumption levels grow large enough, gas transport limitations develop in the diffusion media and catalyst layers. These arise through the normal effective diffusivity of the GDL media and catalyst layers, and are further exacerbated if liquid water accumulates and blocks the pores of the GDL used for gas diffusion. Mass transport losses which arise from reduced reactant concentration, or partial pressures, at the reaction sites within the catalyst layers can be estimated from the Nernst equation (6). With the inability to supply reactants at required rates, the

voltage curve turns down precipitously, which is indicative of large overpotentials leading to a limiting current density value.

2.1 Fuel Cell Stacks

For any single cell, the operational voltage has been found to be in the range of 0.6 to 0.7 V, therefore, cells have to be stacked together in series to build a working engine. The flow channels are within bipolar plates which supply the anode on one side and the cathode on the other. Figure 3 shows a picture of a 5-cell stack. Practical stacks use many more cells. For example in automobile applications [15], stacks with 200

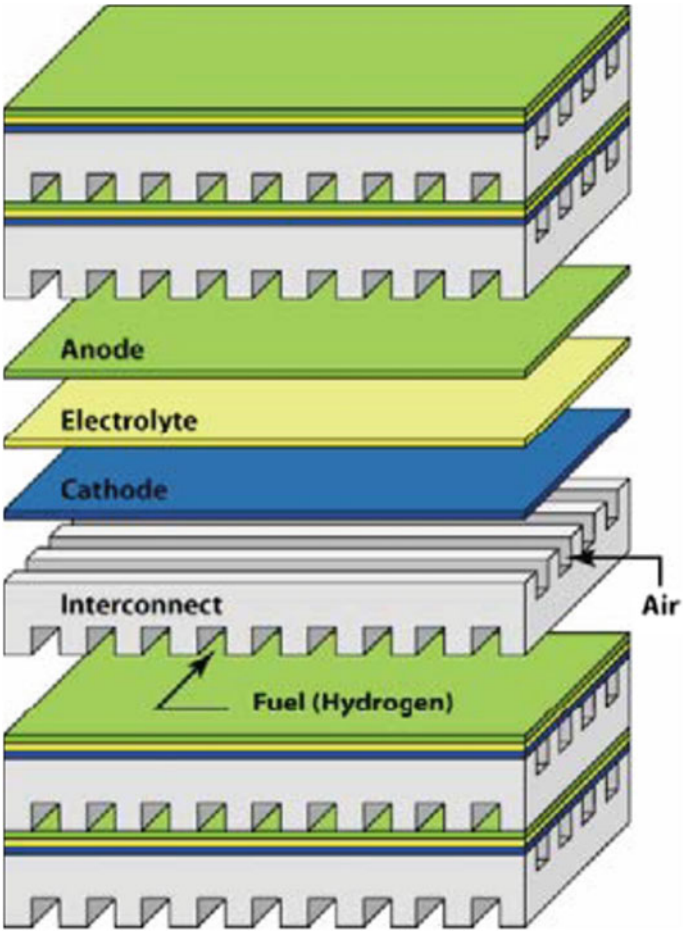

Fig. 3 5-cell polymer electrolyte membrane stack, showing bipolar plates

cells are not uncommon. With an active cell area of 500 cm^2, total power of 60 kW could be delivered, assuming 1 A/cm^2 current density. In these cases, with tightly packed cells, thermal and water management are of critical concern, requiring in some cases, extra cooling channels. Design and flow patterns in bipolar plates are also critical to ensure adequate supply of reactants to the GDL and reaction sites [16].

3 Mathematical Model

The governing equations typically used to model a PEM fuel cell with computational fluid dynamics are presented. They are equations of flow, heat transfer, and current conduction. The flows are laminar and involve variable properties, such as density. In the porous diffusion media, the Brinkman equations solve for fluid velocity. The solid and fluid phases are assumed to be in thermodynamic equilibrium

The various computational subdomains or regions of the PEM fuel cell are described in Fig. 4 with a cutaway view representing the cross section of a single channel on each side. The divisions mirror the major components of the device.

Gas flows freely through the anode and cathode gas channels and also in the porous regions of the gas diffusion layers (GDL). The GDL has a porosity ε, which is the fraction of a control volume occupied by gas, between zero and 1. Porosity is zero in pure solid regions (the collector plates) and unity in the flow channels. Physical properties of the fluid are averages taken over the volume of the pores. The density and viscosity of the fluid in the porous regions are properties that can be

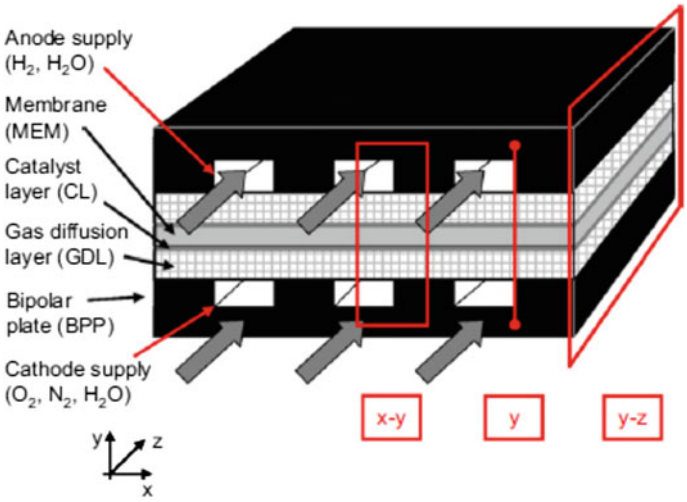

Fig. 4 PEMFC geometry: schematic illustration of different computational domains (1-D—*y*-direction; 2-D—*x*-*y* or *y*-*z* directions; 3-D—*x*-*y*-*z* directions) [17]

measured experimentally in a free flow region and so all properties are continuous with those in the adjacent free flow. The flow velocity in the porous regions is defined as a superficial volume average, or Darcy velocity. This average over a unit volume (entire volume comprising both solid matrix and pore) defines velocity as the volume flow rate per area of the porous medium. When defined this way, the fluid velocity is continuous at gas channel-GDL boundaries.

The continuity and momentum equations (8) and (9), taken together, are known as the *Brinkman equations*, which must be solved to yield the velocity field.

$$\nabla \cdot (\rho \vec{\mathbf{u}}) = 0 \tag{8}$$

$$\frac{\rho}{\varepsilon^2}(\vec{\mathbf{u}} \cdot \nabla \vec{\mathbf{u}}) = -\nabla p + \nabla \cdot \left[\frac{\mu}{\varepsilon} \left\{ \nabla \vec{\mathbf{u}} + (\nabla \vec{\mathbf{u}})^T - \frac{2}{3}(\nabla \cdot \vec{\mathbf{u}}) \bar{\bar{\mathbf{I}}} \right\} \right] - \bar{\bar{\mathbf{K}}}^{-1} \mu \vec{\mathbf{u}} \tag{9}$$

where μ (kg m^{-1} s^{-1}) is the dynamic viscosity of the mixture, $\vec{\mathbf{u}}$ is the mass-average velocity vector (m s^{-1}) in the Cartesian coordinate system, $\bar{\bar{\mathbf{K}}}$ is the permeability tensor of the porous medium.

The conservation of species equations are applied to the same domains and represent mass flux from convection and diffusion, as well as sources which arise from phase change and/or electrochemical reactions. The cathode gas has three species (oxygen = 1, water = 2, and nitrogen = 3) and the anode uses two species (hydrogen = 1, water = 2). The mass fractions ω_i of species i at the cathode are given by Eq. (10) where $\widetilde{D}_{ik}$ ($i, k = 1, 2, 3$) are the multicomponent Fick Diffusivities, the components of the multicomponent Fick diffusivity matrix, which are needed to solve the problem. These are symmetric, i.e., $\widetilde{D}_{ik} = \widetilde{D}_{ki}$. The multicomponent Fick Diffusivities are determined from the multicomponent Maxwell–Stefan diffusivities D_{ik}.

$$\begin{aligned} \nabla \cdot (\rho \vec{\mathbf{u}} \omega_1) &= \nabla \cdot \left[\rho \omega_1 \sum_k \widetilde{D}_{1k} \left(\nabla x_k + \tfrac{\nabla p}{p}(x_k - \omega_k) \right) \right] \\ \nabla \cdot (\rho \vec{\mathbf{u}} \omega_2) &= \nabla \cdot \left[\rho \omega_2 \sum_k \widetilde{D}_{2k} \left(\nabla x_k + \tfrac{\nabla p}{p}(x_k - \omega_k) \right) \right] \\ \omega_3 &= 1 - \omega_1 - \omega_2 \end{aligned} \tag{10}$$

where x_k represents the corresponding mole fraction.

The heat transfer is governed by Eq. (11)

$$\nabla \cdot \left(\rho c_p \vec{\mathbf{u}} T - k_{\text{eff}} \nabla T \right) = Q \tag{11}$$

where

$$k_{\text{eff}} = (1 - \varepsilon) k_{\text{GDL}} + \varepsilon k \tag{12}$$

The thermal conductivity of the GDL material is strongly anisotropic, with in-plane ($k_{\text{GDL},=}$) and thru-plane ($k_{\text{GDL},\perp}$) values. It is represented by a tensor

$$k_{\mathrm{GDL}} = \begin{bmatrix} k_{\mathrm{GDL},=} & 0 & 0 \\ 0 & k_{\mathrm{GDL},=} & 0 \\ 0 & 0 & k_{\mathrm{GDL},\perp} \end{bmatrix} \tag{13}$$

Significant thermal contact resistances have been recognized as occurring at the current collector plate and the GDL. At other component interfaces, contact resistances are commonly ignored [18]. Thermal contact resistance between multiple layers of GDL was found to be negligible [19], and the contact resistance with solid plates (R_{ct}) was found to be about 1–1.5 $\times$ 10^{-4} m^2 K/W at typical cell compaction pressures.

The conservation of electron charge equation must be solved in the electronically conductive domains. Voltage losses arising from electronic conduction have been ignored in many models; thought to be insignificant due to the high electrical conductivity of the respective materials. Current flux $\overrightarrow{\mathbf{J}_e}$ in Eq. (14) (A m^{-2}) is represented as the flow of positive charges in the direction of reduced electrical potential, in the presence of an electric field $\overrightarrow{\mathbf{E}}$ (V m^{-1}), and current must be conserved as Eq. (14) where Φ_e is the scalar electric potential and σ_e (S m^{-1}) the electrical conductivity. The electrical conductivity of the current collector plate (CCL) is isotropic, but that of the GDL is a tensor: it has separate in-plane ($\sigma_{e,=}$) and thru-plane ($\sigma_{e,\perp}$) values as in Eq. (15)

$$\nabla \cdot \overrightarrow{\mathbf{J}_e} = \nabla \cdot \left(\sigma_e \overrightarrow{\mathbf{E}}\right) = \nabla \cdot (\sigma_e(-\nabla \Phi_e)) = 0 \tag{14}$$

$$\sigma_e = \begin{bmatrix} \sigma_{e,=} & 0 & 0 \\ 0 & \sigma_{e,=} & 0 \\ 0 & 0 & \sigma_{e,\perp} \end{bmatrix} \tag{15}$$

Thru-plane resistivity values of 0.08 (Ω cm) and in-plane resistivity values of 0.006 (Ω cm) have been reported as typical [20]. In the catalyst layers, current production is governed by the Butler–Volmer relations [21]. Thus the charge equations for the electron and proton transport in the solid and electrolyte media, respectively are

$$\nabla \cdot (\sigma_s(-\nabla \Phi_s)) = S_s \tag{16}$$

$$\nabla \cdot (\sigma_{el}(-\nabla \Phi_{el})) = S_{el} \tag{17}$$

where the source terms in the Anode Catalyst Layer are

$$S_s = -j_a;\ S_{el} = j_a; \tag{18}$$

and the source terms in the Cathode Catalyst Layer are

$$S_s = -j_c;\ S_{el} = j_c; \tag{19}$$

j_a, j_c are the local current density at the anode and cathode sides, respectively, given by the *Butler–Volmer relations*

$$j_a = \left(a i_o^{\text{ref}}\right)_a \left(\frac{P_{\text{H}_2}}{P_{\text{H}_2}^{\text{ref}}}\right)^{\frac{1}{2}} \left[\exp\left(\frac{\alpha_a^a F}{RT}\right)\eta_a - \exp\left(\frac{-\alpha_c^a F}{RT}\right)\eta_a\right] \tag{20}$$

$$j_c = \left(a i_o^{\text{ref}}\right)_c \left(\frac{P_{\text{O}_2}}{P_{\text{O}_2}^{\text{ref}}}\right) \left[\exp\left(\frac{\alpha_a^c F}{RT}\right)\eta_c - \exp\left(\frac{-\alpha_c^c F}{RT}\right)\eta_c\right] \tag{21}$$

where a is the electrocatalytic surface area per unit volume and η_a and η_c are overpotentials and i_o is the corresponding exchange current density, at the anode and cathode, respectively.

Resistive heating gives a minor volumetric heat source Q (W m^{-3}) from the dissipation of electrical energy within the conductive GDL and CCL domains described by Eq. (22)

$$Q = \vec{\mathbf{J}}_e \cdot \vec{\mathbf{E}} \tag{22}$$

In summary, the total number of conservation equations are 8 (anode) or 9 (cathode) scalar equations for the same number of unknown variables to be solved for. The continuity and momentum equations give the pressure p and the three components of $\vec{\mathbf{u}}$. The conservation of species equations give the 2 scalar mass fractions in the anode domain, with variables $\omega_1 = \omega_{\text{H}_2}$ and $\omega_2 = \omega_{\text{H}_2\text{O}}$, or the 3 scalar mass fractions, with variables $\omega_1 = \omega_{\text{O}_2}$ and $\omega_2 = \omega_{\text{H}_2\text{O}}$, and $\omega_3 = \omega_{\text{N}_2}$, on the cathode side. The conservation of energy equation gives the scalar variable T (temperature) and the remaining conservation of electronic current equation gives the scalar potential Φ_e. This system of equations is solved by standard CFD methods [11, 17], many of which use the SIMPLE algorithm [22], or one of its many derivatives (SIMPLER, SIMPLEC, PISO, etc.).

4 Methodology Review

4.1 Empirically Based 0-D Models

The earliest experimental studies of the PEM fuel cell typically involved determination of the polarization curve, the measure of its performance. This is done under specific test conditions such as cell temperature, and reactant gas flow rates and humidity levels. As voltage levels are synonymous with efficiency, such comparisons have direct validity. In a recent paper, Wilberforce et al. [23] used measurements to analyze the performance of a 5-cell stack, under varying conditions of temperature and oxygen supply pressure. Figure 5 shows variations in OCV, stack current,

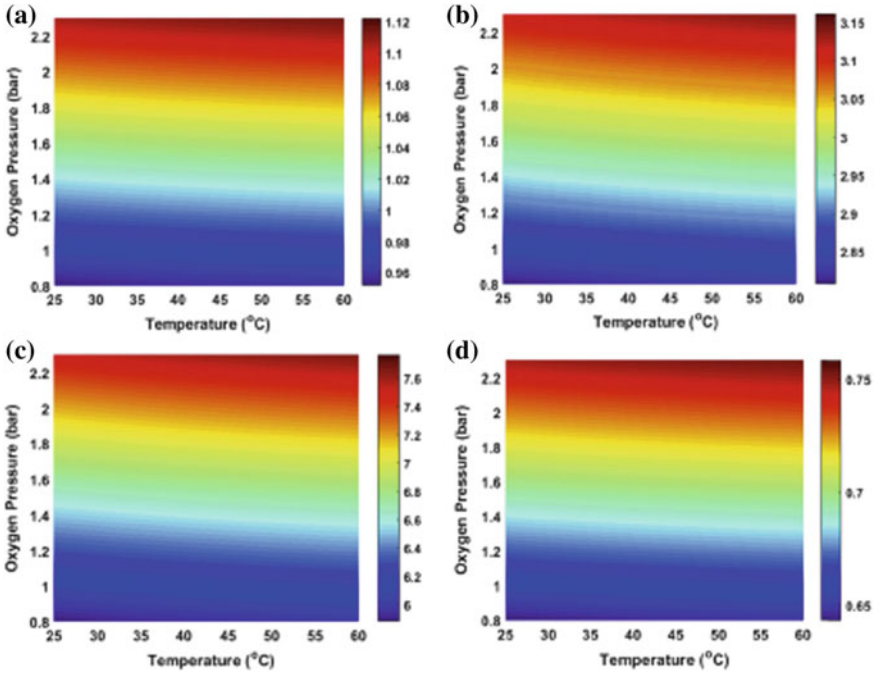

Fig. 5 Measured data for 5-cell PEMFC stack with constant hydrogen pressure of 2.5 bar; **a** open-circuit voltage (V), **b** stack current (A), **c** maximum power (W), **d** fuel cell efficiency [23]

maximum power and efficiency, derived from the data. Performance increases with oxygen gas pressure, as expected from the Nernst equation (6). Furthermore, at any given gas pressure levels, performance improved with increase in temperature. This can be explained with the increased activity level, and corresponding decrease in activation losses, with temperature rise in the cells.

In these zero-dimensional (0-D) models, the measured curve was compared against the thermodynamic voltage, and several mechanisms of voltage losses assessed from the measured data. The polarization curve can usually be fitted with a number of empirical functions that estimate the open-circuit voltage, along with average values of the different loss effects [6, 24], such as gas crossover, kinetic losses, ohmic losses, and mass transport effects. One example of this approach illustrated how the shape of the curve indicates different fundamental loss mechanisms, where one loss mechanism was clearly dominant in various current density ranges [25]. 0-D models are not true predictive models but serve as empirical fits of the experimental observation, indicative of expected performance. Laurencelle et al. [26] found a good correlation fit for the experimental data of the polarization curve. Cooper et al. [27] concluded that the status of these "characterization" equations is settled, and that the analysis and fitting procedures are unlikely to experience significant further development.

Experimental data are of utmost importance in calibrating and validating CFD models. Distributed diagnostic measurements have been developed to provide benchmark data for fuel cell model validation. The term distributed diagnostics refers to the efforts to measure local spatial variations in temperature, current, cell resistance or conductivity, species concentration, etc. These tools are ideally used to validate multidimensional models. Local polarization curves have been produced [28] from a small portion of a segmented cell. Current mapping is commonly used as a term to describe distributed current density measurement. Distributed current density measurements were identified as a key to understanding fuel cell systems [29], where very small cells were found to have nearly uniform current distribution, and larger area cells would have variations in current density, oxygen concentration, humidity, water flooding, and/or temperature. The measurement techniques began with magnetic loop arrays that are embedded in the current collector plates [30, 31]. This technique has the advantage of being done independently of cell operation, but can only be used with a single cell: it is not compatible with fuel cell stacks. Other approaches involved using segmented cells: individual cells that were electrically isolated from each other. These segmented cells could provide spatial resolutions about the size of a single gas channel [32]. Some of these approaches have been criticized in that a segmented MEA will disrupt the current distribution reaching the current collectors, thus giving a measurement that is not indicative of the full-sized MEA. On the other hand, Mench and Wang [29] used an un-altered MEA with an electrically segregated (segmented) flow field.

Distributed temperature and species measurements have been used for evaluating model agreement. Attempts to measure the thru-membrane temperature profile have involved embedding thermocouples in the diffusion media of a PEMFC [33], as well as embedding micro-thermocouples between two layers of membrane sheets [34, 35]. Temperature measurements were plotted at discrete points along the length of the serpentine flow path. These works showed that commonly used isothermal assumptions are not well justified at high current densities, as temperatures varied as much as 10 °C within the electrolyte. Species distribution was determined with a gas chromatograph which measured mole fractions of the various species present in the gas channels of an operating PEMFC [36]. This allowed for an experimental verification of the water vapor mole fraction in the PEMFC flow-fields at steady state. Measurements could only be taken about every 2 min, but this technique was not workable in the presence of liquid water. Later the same group combined in situ data measurement of species distribution, current distribution, and high-frequency resistance distribution with improved transient response to nearly reach real time (1 s per point) [37]. Edwards and Demuren [38] measured transient response of a PEM fuel cell to step changes in load current under various conditions of temperature and humidity. They found good correlation with a triple-term exponential curve fit. The first and fastest time scale is associated with hydration effect on protonic resistance in the catalyst layers. The second, which is one order of magnitude slower is associated with hydration effect on protonic resistance in the electrolyte. And the third time scale, which is two orders of magnitude slower is consistent with effects of heat generation in the MEA on activation losses.

4.2 Electrochemical and Transport Model Calibration Studies

Reactant crossover measurement is relevant to PEMFC modeling because the reactant crossover, or leakage, reduces the open-circuit cell voltage (OCV) by a noticeable amount from the reversible voltage or "Nernst" value. There are several methods to determine gaseous reactant (hydrogen) crossover through the proton exchange membrane. Accounting for crossover can be done by adding a crossover current to the model for kinetic losses or with an arbitrary reduction in the OCV of a fuel cell. The crossover is usually unresolved; i.e., it is assumed to be spatially averaged over the area of the MEA. In situ electrochemical methods for measuring crossover include cyclic voltammetry (CV) [39] and linear sweep voltammetry (LSV) [27]. Crossover can be measured directly, and levels of 1–2 mA/cm^2 are thought to be typical. LSV can also detect the presence of an internal short-circuit through the presence of a positive slope of the current/potential curve.

Active Surface Area Measurement typically uses CV in fuel cell studies to measure the electrochemically active surface area (ECSA) of catalyst layers. ECSA testing is used to evaluate the performance of catalysts, modifications to catalyst layer microstructure(s) and/or catalyst loading, and the presence of adsorbed surface poison. CFD models use either ECSA or exchange current density estimates to calculate kinetic losses of both the anode and cathode [40, 41]. They are often not known precisely and have been treated as parameters which are adjusted to align model predictions with experimental data. Typically, area values are reported with respect to the catalyst loading. Values of around 50 m^2/g Pt [24], with ordinary platinum catalysts, are reported in well-designed PEMFC cathodes. ECSA values have been found, experimentally, to drop with decreasing humidity and/or ionomer volume fraction [42], and most CFD models have failed to account for this.

Ohmic Losses in the PEMFC are comprised of ionic resistance losses (mostly from the electrolyte), electronic contact resistances between components, and bulk electronic resistance. Test equipment is now commonly available to make in situ ohmic resistance measurements on an operating PEMFC. The most common in situ methods are the current-interrupt and high-frequency resistance (HFR) methods. These produce the sum of (i) electronic resistances, and (ii) ohmic resistances arising in the membrane of a PEMFC [43]. The two methods are nearly equivalent and have been frequently used for kinetics research and as a validation aid.

It is typically desired to separate the ohmic resistance components. Electronic resistances might be implicitly assumed to be negligible or may be measured separately (ex-situ) within a "dummy" cell (one where the MEA has been removed). This latter procedure was used in kinetics research [40, 41, 44]. The previously mentioned in situ methods do not address, or include, catalyst layer ionic and electronic resistances. Further research has been focused on experimentally assessing ionic resistance losses in catalyst layers [45]. Ionic conduction losses have been shown to be significant, while electronic conduction losses within PEMFC catalyst layers have frequently been considered negligible [41, 46].

Diffusional Losses in Catalyst Layers have been investigated. In an operating PEMFC, reactant gases must move through some portion of the thickness of each catalyst layer to reach the available reaction sites. This process was thought to be dominated by diffusion instead of pressure-driven flow [24], and so significant experimental and modeling research has been invested to develop accurate gas diffusion transport models, applicable to the catalyst layer composition. As hydrogen has a greater diffusional coefficient, and anode losses are not typically as significant, most effort has focused on oxygen diffusion through CCL media. Key early works investigated the microstructure of catalyst layers, finding that there existed two distinct pore size distributions within typical CL structures, and that pore sizes were between nanometer and sub-micrometer [47, 48]. The larger pores tended to be partially filled with ionomer, with the effect that oxygen diffusion coefficient decreased as ionomer loading increased [49] and thus the performance of the MEA suffered. On the other hand, computer models used much higher oxygen diffusion coefficients in PEMFC catalyst layers. Estimates of effective values were in the range 0.1–0.3 $cm^2\ s^{-1}$ at 80 °C, which justified ignoring these diffusional losses [50, 51]. Experimental measurements of effective diffusion coefficients were taken in 2005 to be in the range 0.006–0.007 $cm^2\ s^{-1}$ at 80 °C [52], from evaluation of a typical CL structure. In a 2010 study, measured effective diffusion coefficients dropped from 0.024 to 0.001 $cm^2\ s^{-1}$ at 80 °C as ionomer loadings and humidity were increased [53]. Later measurements, in 2011, found a value of 0.002 $cm^2\ s^{-1}$ at 80 °C [54]. The Bruggeman correction, which was commonly used for estimating effective diffusion coefficients of porous catalyst layers, was found to underestimate catalyst layer tortuosity [53, 54].

Pore size distributions within the CL structures were found to be similar to the mean free path of oxygen molecules. Inaccessible pores were present, which reduced the porosity by 20–60% from the value which was expected, based purely on density calculations. Oxygen diffusion was found to take place within the "transition region" where both Knudsen and molecular diffusion must be taken into account [54]. By 2012, experimental measurements at 0% RH were shown to be consistent with such a model of diffusion, when porosity and tortuosity effects were properly assessed [55]. The presence of inaccessible pores in the CL structures served to reduce porosity and the effective diffusion coefficient. Intensive, pore-scale models have been developed based on these findings. These models are intended to serve as a valid analytical basis for macro-homogeneous models, providing effective transport properties. They computationally reconstruct catalyst layer microstructures and then devise effective transport properties. The choice of pore-scale models (referred to as a reconstruction algorithm) did not substantially affect effective transport properties that these models were to predict [56]. It was more important to account for the reduced porosity [57] resulting from Nafion loading.

Electrode Kinetic parameter estimation research has progressed significantly. Both anode and cathode electrodes are expected to continue utilizing the current carbon-supported platinum (Pt/C) technology [58]. CFD models require kinetic data to estimate voltage or efficiency losses occurring in these reactions. Each follows Butler–Volmer kinetics [20, 24], where the reaction rate is described by two parameters: (i) exchange coefficients and (ii) exchange current density. Many CFD models

presented kinetic values without clear justification, treating these as free parameters which are adjusted to produce agreement between model and experimental data. Kinetic model parameters, such as exchange current density, are sometimes discussed in terms of the electrochemically active surface area (ECSA), which is then related to catalyst loading. The practice in several studies is to use kinetic model parameters devised with consideration of ACL/CCL composition.

The hydrogen oxidation reaction (HOR) occurring at the anode is quite facile (rapid). Under these conditions, the Butler–Volmer relations, simplify to linear kinetics [24]. Voltage losses are typically very small, often too small to measure. Experimental results suggest the possibility to lower the anode platinum catalyst loading, thereby saving cost, without significantly degrading performance [59]. Estimates of the HOR kinetics parameters available in 2007 were compared and found to show variations of orders of magnitude. Neyerlin et al. [44] presented HOR kinetics parameters from a H_2 pump test, with the suggestion that the prior rotating disk electrode (RDE) experiments were compromised by unacknowledged mass transport limitations. Butler–Volmer model parameters could only be determined from experimental data to within a factor of 2. Durst et al. [58] offered more precise kinetic data estimates and developed temperature-dependence as well.

The oxygen reduction reaction (ORR) occurring in the cathode is more complicated and much slower, and voltage losses from it are more substantial. Under these conditions, the Butler–Volmer relation, Eq. (21), reduces to Tafel kinetics, Eq. (7) [20, 24], where a Tafel slope, reaction order, and exchange current density are required. Substantial work has gone into cathode catalyst layer development and the characterization of the cathode ORR reaction. The cathode reaction follows Tafel kinetics with reaction order (with respect to oxygen concentration) of about 0.5 [60]. There has been a substantial disagreement in modeling the cathode reaction between much older and more recent works. Experimental work combined with intensive microscale modeling was able to explain how previous experiments produced kinetic data with double the theoretically correct Tafel slope due to undiagnosed ionic conduction losses in the cathode catalyst layer and unrealized gas diffusion limitations [61]. The suggestion of these and later workers is that older rotating disk electrode (RDE) kinetic experiments and the derived data are in some doubt. Wang [51] presented calculations in 2007 which showed how the oxygen concentration levels, temperature, and ionic conductivity within typical cathode catalyst layers could be considered uniform. Ionic conductivity, however, was still highly hydration dependent. Neyerlin and Gu [40] improved the ohmic loss compensation techniques to better measure in situ ORR kinetic data. Later works extended the technique to account for incomplete catalyst layer utilization [41], which occurs under high current density and/or low humidity operation when effective catalyst layer resistances become significantly large. Wang and Feng [50] expanded the analytical solutions used by Neyerlin et al. [40]. By 2009, Liu et al. [45] verified the correctness of these solutions by testing a range of electrode compositions with different humidity levels. The ionomer volume fraction of about 0.13 ($I/C > 0.6$), and relative humidity of 30% [62], were consistent with the analytical solution for cathode catalyst layer performance. These values mirror most typical catalyst layer compositions.

With recognition/compensation of appropriate catalyst layer resistance, a model of ORR kinetics could be devised that is consistent across different operating conditions. Experimentally determined ORR kinetics were found to be almost independent of humidity and electrode composition and Pt catalyst loading. The remaining loss, attributed to humidity variation in typical operational conditions, can be explained by the experimentally observed shift in ECSA from humidity alone [42]. Thus, a model of ORR kinetics was presented that is consistent with and viable across different operating conditions and catalyst layer compositions. CFD models that do not account for cathode catalyst layer resistances can still match experimental polarization data fairly well, and even while operating at low humidity conditions where catalyst layer losses should be large enough to introduce significant error. These models can match experimental *V-I* data by doubling the Tafel slope of the ORR [63] and then treating the exchange current density as a free parameter of the problem, i.e., a calibration choice could be made to match particular experiments, even with neglect of the underlying physics of the CCL catalyst loading.

Water Transport in PFSA Membranes has been an area of active investigation. Water Transport models mostly follow two very distinct modeling approaches: the hydraulic model of Bernardi and Verbrugge [64] and the "diffusive" approach of Springer and Zawodzinski of Los Alamos National Laboratory [65]. The latter approach is used by most CFD models. By 2008, the diffusive approach was the de facto model in commercial software [66]. Many works reported membrane water transport property values devised mostly ex-situ. These have had the goal of measuring water sorption, membrane conductivity, water diffusion coefficients, and electroosmotic (EO) drag coefficients following the "diffusive" model framework. The intention was that diffusive models used in CFD simulations would be more useful and accurate with appropriate transport parameters (property values).

The "diffusive" approach begins with determination of an equilibrium water uptake value. Zawodzinski et al. [67] measured equilibrium water uptake curves from membranes exposed to humidified gas and liquid water. They developed an empirical fit for water content as a function of water activity (relative humidity) based upon weight gain data for selected membranes. This was supported with data from both liquid water uptake and vapor phase uptake [68]. Hinatsu et al. [69] refined the apparatus for these measurements and reported water uptake data by Nafion with liquid through a range of temperatures, as well as the vapor-equilibrated uptake curve through 80 °C. Improved measurement data were reported by Jalani et al. [70]. Onishi et al. [71] examined water uptake in more detail, raising the possibility that prior water uptake data were dependent upon "*thermal history,*" and that many water uptake studies might have been influenced by these effects. Kusoglu et al. [72] investigated the influences of geometrical constraint and compression upon water uptake. The previous water uptake curves were mostly empirical in nature, with expressions made to fit the experimental data.

Previous investigations of membrane ionic conductivity had shown that a strong dependence on water content could be expected. Zawodzinski et al. [68] were able to measure conductivity levels which exhibited linear dependence on water content at 30 °C. Halim et al. [73] also conducted conductivity experiments, using AC impedance

measurements of liquid-equilibrated membranes. They found similar activation energies for multiple membranes and that the variation of conductivity with temperature followed the Arrhenius law. Though these early relationships still appear to be in use in CFD models; later works have proposed relationships in which membrane ionic conductivity takes somewhat different forms [71, 74].

The membrane water transport model of Springer and coworkers [65, 67, 68] requires a self-diffusion coefficient of water, and an electroosmotic drag coefficient (representing the number of water molecules carried with each proton that crosses the membrane). Both are temperature and water content dependent. Attempts to measure these parameters have generated much disagreement between various groups and authors. The earliest work, from 1991 where Zawodzinski et al. [67] used pulsed-field gradient spin-echo ‘H NMR measurements of ‘H intradiffusion coefficients in Nafion 117 membranes (in the absence of a water concentration gradient). Measures of electroosmotic drag were also reported as being 2.5 (liquid-equilibrated membrane) and 0.9 (vapor-equilibrated membrane). Motupally et al. [75] reported permeation experiments to measure water diffusion. Their empirical correlation is used in many CFD models for the diffusion coefficient. Note that this work assumes the validity of the equilibrium assumption: water uptake data from equilibrated membranes is used to assign water content values on opposite sides of a membrane during permeation experiments. The experiment limited itself to one particular membrane thickness. A multitude of approaches has been used to estimate the electroosmotic drag, such as a hydrogen pumping cell by Ye and Wang [76]. The transport parameters, however, were subject to a great deal of disagreement based on the method used and results obtained, as indicated by Ge et al. [77]. Nevertheless, there was general agreement that the resulting water content profile in thin (50 μm) membranes was nearly linear and anode dryout was not expected in the thin membranes [76].

Membrane Water Content Imaging techniques have been refined over the years. Some of these works attempted to validate the membrane water transport models in situ. Buchi and Scherer [78] made membrane resistance measurements in an operating fuel cell with a known, thick composite membrane. Membrane resistance was found to increase significantly with current density, which was attributed to the drying out of the membrane on the anode side. A later work, by the same authors [79] used distributed local resistance measurements from evenly spaced points between the anode and the cathode. Drying out effects could clearly be seen where the membrane resistances increased at the anode side as current density increased. The effect was more pronounced with thicker membranes and less noticeable in the thinner ones. The characteristic drying out of the membrane on the anode side was observed. This was caused by the nonlinearity of the water transport in the membrane, and the variation of the diffusion coefficient with water content. However, only a qualitative agreement of diffusive models with the experimental data was achieved [80].

Further sorption/desorption (wetting and drying) experiments, performed on Nafion membranes, were used to investigate water transport. Nafion membranes had very flat water content profiles as they gained or lost water; the rate of water redistribution within the membrane was found to be much faster than the water loss.

It was also seen that the uptake of water is an order of magnitude faster in the presence of liquid water, compared to water vapor. In both liquid/vapor cases the sorption kinetics are controlled by the transfer process at the membrane surface [81, 82]. Water content equilibrium values were seen to match previously determined sorption curves via gravimetric tests [83]. Imaging was done during permeation and operational fuel cell experiments, which utilized micro-Raman spectroscopy found the presence of significant interfacial resistance, influenced by temperature and humidity. The local water content at the edges of the membrane was not in equilibrium with the water activity in the gas phase during these permeation experiments. In all cases [83, 84], equilibrium water content was slowly reestablished when water flux ceased, and linear water content profiles were observed in steady operation with membranes less than 100 μm in thickness.

Examinations of water content imaging, during permeation experiments, with X-ray microtomography by Hwang et al. [85] suggested the presence of an interfacial resistance to water transport. Operational PEMFC water content imaging measurements with the MRI technique by Tsushima et al. [86] captured the anode side depletion of water as current density increased. Later, in 2010, Tsushima et al. [87] were able to perform MRI measurements in PEMFC at higher realistic operating temperatures, and the technique (environmental MRI or EMRI) was extended beyond most of the earlier works which were limited to room-temperature measurements. This work showed linear water profiles developing as the membrane hydration levels increased. They inferred that the diffusion coefficient of water in Nafion was maximum at dimensionless water content level as low as 3–5. These results call into question the assumption of equilibrium of water content (between the gaseous phase and the membrane water content) employed with most membrane water transport models. That equilibrium assumption has been widely employed in many CFD models.

Nonequilibrium Water Transport in PFSA Membranes was introduced around 2004 by Chen et al. [88] and Berg et al. [89]. They modeled nonequilibrium membrane water uptake rates. The concept was to build a model of water transport in the membrane that was not based on equilibrium absorption from the adjoining water vapor. Instead, the rate of absorption/desorption of water into/from the membrane was driven by a gap or jump in the water content level between the actual water content and that determined by equilibrium sorption values. In 2007 Majsztrik et al. conducted a more thorough series of sorption, desorption, and permeation experiments, with the observation that diffusion was the only one of three resistances to water sorption (interfacial resistance, diffusion, and membrane swelling) to accommodate water uptake [90]. Which resistance was the controlling one was said to vary with humidity, sample thickness, and temperature. Monroe et al. [91] did another group of water permeation experiments and claimed interfacial resistance limits the overall water transfer rates when membrane thickness is less than a critical value of about 300 μm. State-of-the-art membranes are about 30–100 μm thick.

Ge et al. [92] developed mass transfer coefficients which were not constant, but rather were dependent on the local volume fraction of water at the membrane edges. The diffusion coefficient was also modeled as being dependent on the water volume

fraction in the membrane (which is water content dependent). Ge et al. [77] later determined the electroosmotic drag coefficient using measurements in an operational fuel cell. They compared measured and calculated resistance from the membrane to validate the model. The agreement was good over a range of thicknesses and current densities. The membrane property values (correlations) produced were reasonably consistent with prior works. This work neglected catalyst layer effects and losses, and still required meshing and solving conservation equations throughout the membrane. This work also relied heavily upon the water uptake data of Hinatsu et al. [69], which was later called into question by Onishi et al. [71].

Adachi [93] reported experimental investigations of interfacial water transport resistance. Adachi et al. [94, 95] noted significant interfacial resistance in membranes less than 200 μm in thickness. The presence of catalyst layers, on both sides of the membrane, was found to not change water permeation significantly, and so it was suggested that membrane water permeation experiments could be correlated to those of an operating PEMFC.

Transport in diffusion layers (GDL) has been studied extensively. Gas transport in porous materials depends on their porosity, tortuosity, and permeability. The macro-homogeneous models commonly treat the diffusion layers as isotropic [11]. Two nearly equivalent approaches exist for modeling gas transport in these porous materials [9, 52]. Computational works might not use the permeability values supplied by manufacturers, however, because the properties are expected to change under GDL compression. Mench [24] also described how catalyst and microporous layers (MPL) needed to take into account both molecular and Knudsen diffusion.

Electronic conduction in the GDL is often neglected in earlier published CFD models because the commercially available carbon papers have good electrical conductivity. Meng and Wang [96, 97] observed that electron conduction could have significant effects in altering the current density distribution in the second and third dimensions of a PEMFC model. Properties of the electronically conducting phase will be needed, such as the electrical conductivity of that solid phase. It is commonly recognized that these GDL materials do not have an isotropic electronic conductivity: higher values occur in the in-plane than in the through-plane direction [11, 20].

The thermal conductivity of the diffusion media might be similarly anisotropic, though most early works tended to treat the GDL as isotropic. Attempts to measure thermal conductivity of GDL materials intensified, post 2003, when more effort was put into non-isothermal fuel cell modeling. Mench et al. [34, 35] developed an estimate of thermal conductivity of the diffusion media from in situ micro-thermocouple measurements. Soon afterward, several research groups began to use ex-situ direct measurement methods to determine the thermal conductivity of fuel cell materials, particularly the diffusion media. Measurements included thermal conductivity of the GDL media itself, along with its temperature and compression dependence; and also a contact resistance which was itself compression dependent. Khandelwal and Mench [98] found the thru-plane thermal conductivity for a common carbon paper between 1 and 2 W/m K, which decreases with temperature due to the presence of a carbonized thermosetting resin used as a binder. They found thermal conductivity affected by the presence of added PTFE in the GDL as well. They also noted the presence of a

significant thermal contact resistance which asymptotically reached its lowest limiting value with compression pressure of about 2 MPa. Hysteresis is observed in the contact resistance due to the compression and deformation and breakage of the fibers in the media. Models describing the thermal conductivity of porous materials have been compared with this experimental data [99]. Another work examined thru-plane thermal conductivity and contact resistance of GDL materials with varying compression and levels of liquid water [19]. Each changed conductivity significantly. Sadeghi et al. [100] made additional measurements showing an air-pressure dependence. At low gas pressures, the surface contact resistance became greater than internal conduction losses. Finally, Teertstra et al. [101] showed the thermal anisotropy of the GDL materials, with in-plane thermal conductivity levels 10 times those in the thru-plane direction.

4.3 Computational Fluid Dynamics Models

These works might model a single flow channel of a PEMFC, a complete fuel cell, or even a complete stack, consisting of several cells. CFD models are typically characterized, by time or space, as transient or steady state; combined with their scale and dimensionality; as isothermal/non-isothermal and single-phase/multiphase in the treatment of the presence of liquid water. 1-D models consider the direction through the MEA exclusively. These make up the majority of early modeling works. 2-D models additionally consider the direction downstream, or down the flow channel, and 3-D models further consider effects in the cross-flow direction. Some works have varying dimensionality by region. Figure 4 shows a typical orientation of the coordinate systems. 1-D models are in the *y*-direction. 2-D models follow either the *x*-*y* (in-plane or sandwich) or *y*-*z* (along-the-channel) orientations. 3-D models use the full *x*-*y*-*z* coordinate directions.

Most CFD models employ the continuum assumption, so that exact details of material microstructure are neglected. Important sub-regions of the fuel cell such as diffusion layers, membrane, and catalyst layers are handled this way. Diffusion layers are commonly considered as randomly oriented porous structures that are defined by a porosity and permeability. In examining catalyst layers, a porosity and surface area per unit volume might be considered. CFD codes typically use the finite-volume, finite-difference or finite-element method for solving flow and heat transfer equations in both single- and two-phase flow. Electrochemical effects are introduced via add-on modules available for many commercial software packages.

Isothermal models are those that do not consider the presence of temperature gradients within the fuel cell, and thus, do not account for heat transfer. Isothermal models can consider temperature effects, but simply treat temperature as an input to the problem. This assumption is commonly used in early CFD models. Discrepancies in the treatment of liquid water are also common. The simplest approach is the single-phase one, where the total water amount is considered without regard to whether it is in vapor or liquid form. The gas and liquid phases share the same velocity as they

are in the same fluid mixture. Two-phase models consider the treatment of liquid water presence by predicting a liquid saturation. Saturation values greater than zero characterize flooding and reduce the diffusion coefficients in the gas phase. This has been the focus of a tremendous amount of effort in using CFD to model the PEMFC and is considered critical [102]. However, single-phase models are generally considered valid as long as the saturation value of liquid within the GDL is kept small. Thus they are assumed to be appropriate for low-current density and low humidity operations where liquid water production rate is low and is not expected to accumulate [11].

1-D CFD models were developed for PEMFC simulation in the early 1990s by researchers at Los Alamos National Laboratory [65, 68] and at General Motors [64, 103]. They established the methodology for subsequent modeling efforts, in particular for isothermal conditions. With the adjustment of a couple of parameters, they succeeded in predicting polarization curves in agreement with experimental data. They also predicted low levels of catalyst utilization in the CL [103]. Subsequent models [74, 104–107] expanded on the water treatment and thermal management, accounting for two-phase flow and non-isothermal treatment with heat generation and transport. These models gave insight into the average performance of a fuel cell, but are lacking in simulating distributed properties as observed in real fuel cells. Such variations within a cell are important for the optimization of performance of practical fuel cells with large surface areas. On the other hand, 1-D models require manageable number of grid points (~1000), and can produce comparable results of overall performance of PEMFC as 3-D models [108], which require millions of grid points for resolution. Figure 6 shows very similar predictions of polarization curves between the 1-D and 3-D single-phase models. Improved prediction is achieved, not by increased dimensionality resolution, but solely by going to a two-phase simulation model. The degree of calibration and the number of empirical parameters used varied widely from model to model.

2-D CFD models of PEMFC were developed in the late 1990s. They represent the best compromise between 1-D and 3-D models, in terms of computational details and cost [12]. Number of grid points required for resolution increases from the order of thousands to tens to hundreds of thousands. Gurau et al. [109] presented an along-the-channel (y-z), 2-D model of the flow channels and the MEA, which allowed for computation of variation in reactants, hydrogen and oxygen, in the flow channels as the reaction progresses. The model uses the SIMPLE algorithm and a staged solution process. Similar models were developed by Yi and Nguyen [110] and Um et al. [111]. Siegel et al. [112] presented a 2-D finite-element, single-phase model which studied effectiveness of the catalyst layer. It was subsequently extended to study two-phase flow to account for flooding from water production at the cathode [113]. Computational efficiency of 2-D models was utilized for PEMFC optimization studies [12, 114]. These studies combined the CFD capabilities of COMSOL software FEMLAB with the optimization utilities of MATLAB/Simulink.

2-D sandwich (x-y) orientation models were presented in [115–118], which used a variety of commercial CFD software. Sui and Djilali [115] used the CFD-ACE+ software to investigate the coupling between electronic and mass transport in the

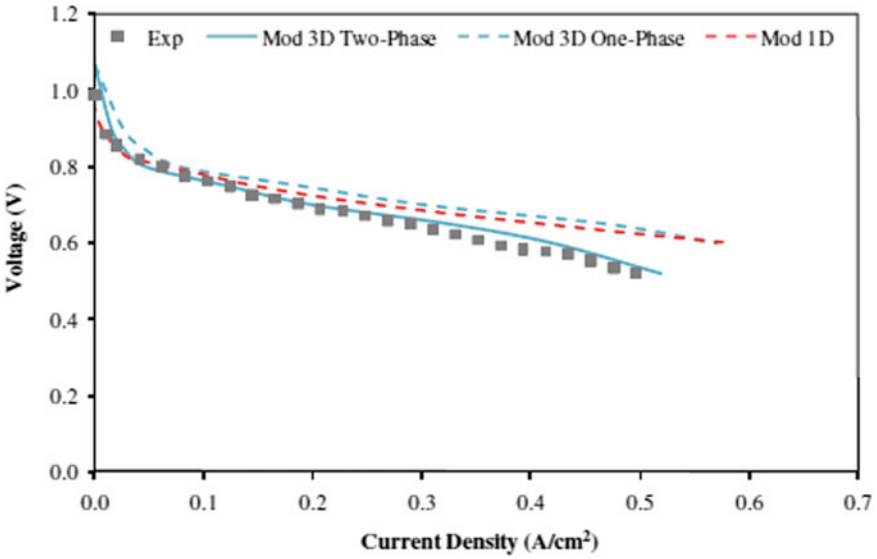

Fig. 6 Comparison of predicted polarization curves for 1-D and 3-D models to experimental data [108]

MEA. They found that either process could be dominant, depending on operating conditions. Losses due to gas crossover effects were investigated by Seddiq et al. [116]. Lin et al. [117] used an existing solver along with an optimization technique, based on the simplified conjugate gradient method to study how the performance of PEMFC is influenced by design parameters such as MEA porosity and flow channel geometry. Meng [118] used FLUENT to solve the transient, non-isothermal, two-phase problem in a PEMFC undergoing a step change in cell voltage, and found that the heat transfer significantly increased the transient response time.

Beale et al. [119] used the PHOENICS [120] code to calculate two-phase flow and mass transfer within the cathode GDL of a PEMFC. A modified version of the interphase slip algorithm (IPSA) [121] was utilized. In this formulation, the liquid and gas flows have different pressures which are determined by solving corresponding Darcy's laws within the GDL.

3-D CFD models of the PEMFC are very computationally intensive, and so are mostly based on commercial codes, with electrochemistry modules built as add-ons. Gridpoints required for adequate resolution of a single cell, in the *x*-*y*-*z* directions shown in Fig. 4, are in the range of hundreds of thousands to several million [17], especially when different arrangements of flow channels have to be simulated. Pourmahmoud et al. [122] detailed the mesh requirements for the single-domain approach with a commercial CFD code. This approach meshes all regions including the MEA (thin membrane and catalyst layers), requiring a large number of cells with high-skew ratio. Altogether, about 60 cells minimum must be used in the MEA through-plane direction, with about 20 grid points to cover the channel width and

~100 points in the flow direction. There are about 20–60 individual channels in the complete flow field, yielding about 6 million points to model even a single small fuel cell [123]. The MEA cells have a very high-aspect ratio, which negatively impacts the solution convergence [66]. Wu et al. investigated MEA meshing requirements as well [124]. An overly fine computational mesh (used in the through-plane direction) caused the solution to become unstable. The number of nodes used in the in-plane directions had much less effect on stability. Figure 7 shows a picture of the typical regions that need to be meshed in a complete model of a single cell [125].

Zhou and Liu expanded the earlier two-dimensional work of Gurau et al. [109] to three dimensions [126], which was later extended with a multiphase mixture formulation by You and Liu [127, 128]. Shimpalee and coworkers, presented 3-D interface models [9, 129], based on the commercial CFD package FLUENT, with added user-coded modules. A later work added 2-phase water treatment [130]. Membrane and catalyst layers, the MEA, was not meshed in these works but was treated as an interface, with zero thickness, separating the anode and cathode flow-fields. Water transport and ohmic potential drop across the MEA were treated with simplifying linear approximations. Calculations then established the water flux and ohmic drop between the anode and cathode and created source terms on both sides of the interface to produce (i) reactant consumption/product creation, (ii) water flux, and (iii) ohmic loss. Sui and Djilali [131] compared computed results of water flux from a single-domain model to those from the interface model of Shimpalee and coworkers. They found significant discrepancies in the presence of large gradients in water content. Errors were said to arise from the diffusion term, and were greater in the thinner membranes than in thicker ones; (diffusion is stronger relative to electro-osmotic drag in the thinner membranes). Mazumder [132] showed that a linear water content profile was appropriate for diffusion dominated drag effects in the membrane; i.e., for thin membranes. Edwards [10] has formulated an improved interface model which uses corrected formulations of the HOR and ORR kinetics and water transport within the MEA.

Um and Wang [133] presented a single-domain approach that utilizes a single set of governing equations in all sub-regions of the fuel cell, avoiding the use of an interface model. The initial model was isothermal and single-phase. Later, Um and Wang [134] added a detailed MEA submodel where the water content distribution within the membrane was resolved. Spatial variations in ionic resistance and reaction rate within the catalyst layer were observed. Wang and Wang [135] expanded the model with the addition of a variable flow model, with mass source terms in the continuity equation and variable gas density in the momentum equations. Mass consumption terms impacted the anode flow field by reducing the pressure drop in a serpentine flow channel.

Computational models need to be properly validated, but experimental data is mostly lacking in details. Recently, distributed current density data, measured in a 10×10 grid in a PEMFC as was used to validate the 3-D model of Wang and coworkers [136]. Results show significant variation in current density between gas inlet and outlet regions. Deviations between data and simulation were generally within $\pm 20\%$. Figure 8 shows comparison of cell polarization curves and deviations

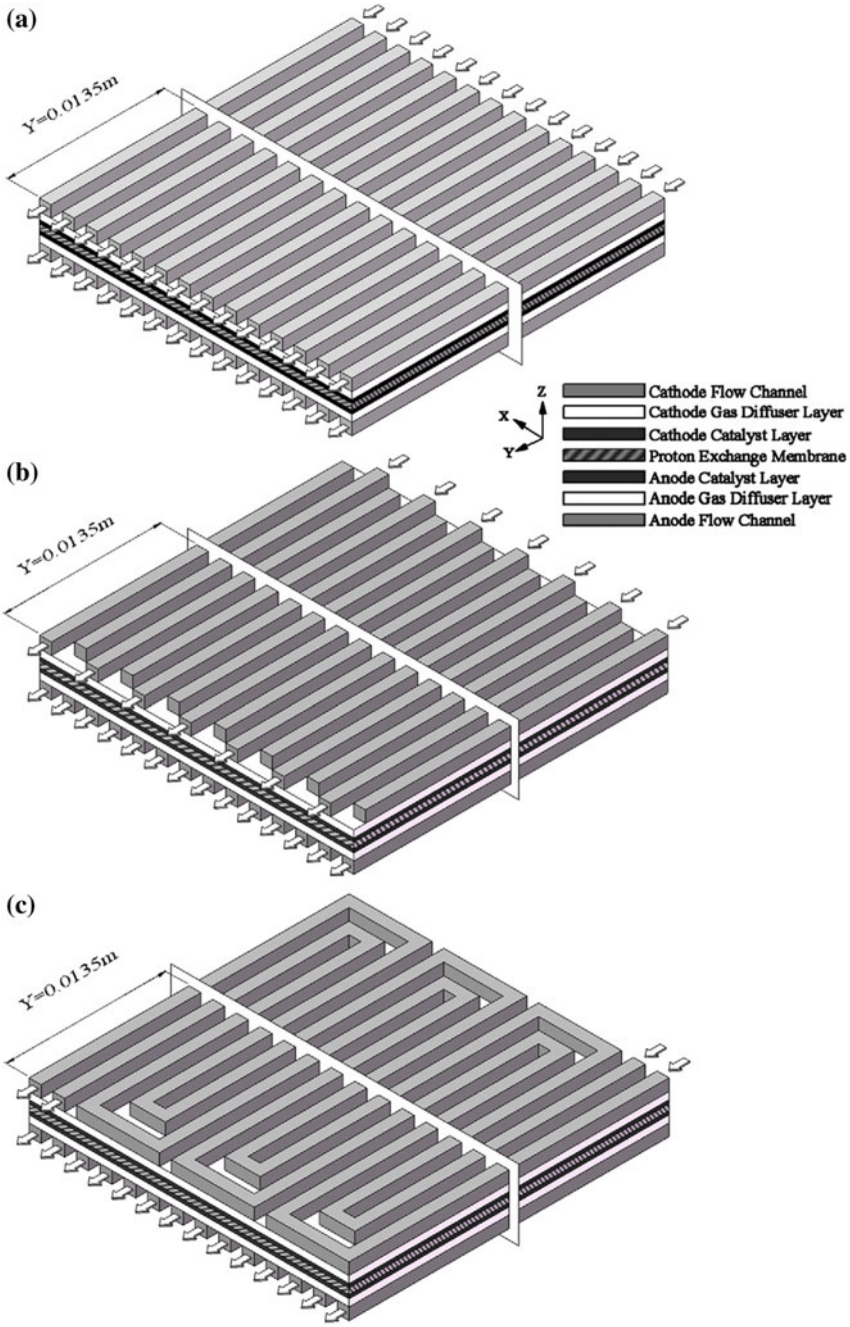

Fig. 7 Single fuel cell with different flow channel arrangements **a** parallel, **b** interdigitated, **c** serpentine [125]

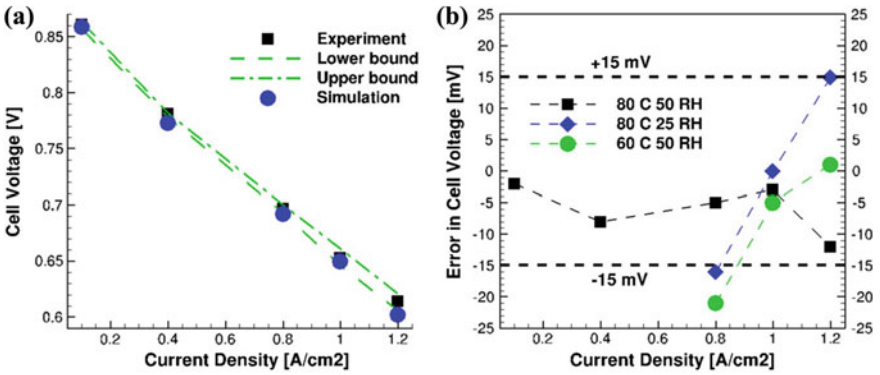

Fig. 8 Comparison of distributed (10 × 10) cell test data with simulation; **a** polarization, **b** error in cell voltage [136]

in cell voltages, three different test conditions, varying temperature, and relative humidity.

Figure 9 shows the distribution of the relative errors in local values of current density, between simulation and measured data, at two average current densities. Largest errors are found near the gas inlet (top), and the gas outlet (bottom). Other 3-D models will benefit from this type of validation effort.

Non-Isothermal models consider heat transport and solve an additional conservation of energy equation. Thermal management is intertwined with water management through temperature effects, whereby the membrane water content depends on the relative humidity of gases, and the saturation pressure of the gases is an exponential function of temperature. Bvumbe et al. [137] considered different modes of heat generation in the MEA. Berning et al. studied thermal management and how different heating terms affected various loss mechanisms [138]. The catalyst layers contain

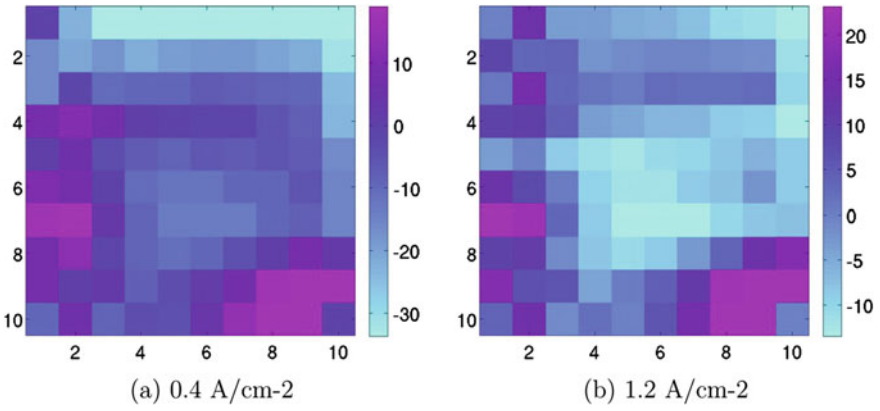

Fig. 9 Relative errors in local values of current density at 80 °C and 50% RH [136]

reversible and irreversible heat terms, and joule heating (ohmic heating) which must be considered. Temperature distributions will depend on the thermal boundary conditions of the model, as well as the thermal properties (i.e. thermal conductivities) of various materials such as the diffusion layer and bipolar plates. The temperature distribution affects water management. Higher temperatures encourage dryout, especially at the anode, with attendant increase in protonic resistance. But at high current densities, water production at the cathode may lead to flooding, thereby impeding adequate supply of oxygen to the cathode. The model of Mazumder and Cole [139, 140] omitted diffusion or electro-osmotic drag in the membrane phase, and also water transport. Models which assume a constant membrane hydration [141] essentially ignore the transport of water and thus predict constant ohmic loss in the PEMFC membrane. They fail to reproduce experimentally observed reduction in membrane ohmic resistance (water gain) at low humidity and high current operation. Likewise, the increase in membrane ohmic resistance with high current density, under high humidity conditions. Some CFD models such as Schwarz and Beale [142] focus on multiphase effects by modeling diffusion in microporous layers, without the difficulties of modeling in the MEA layer. Others have proposed a multiscale approach in which first a CFD model is used for the largest scales of the problem, the macroscopic scales, where problems of heat and mass transfer are solved. But microstructural effects such as pore-filling are used to model water transport throughout the fine, small-scale structure of catalyst layers [143]. The effects of very fine catalyst layer structure (of too small a scale to be resolved by the macroscopic CFD model) on PEMFC performance are handled by mesoscale models.

Commercial CFD software have been used to solve the PEMFC problem in one-two- or three-dimensions. FLUENT appears to be the most popular, with its available fuel cell module or subroutines. It has been used for both 2-D and 3-D simulations. COMSOL Multiphysics (FEMLAB) has also been widely used for 1-D, 2-D, and 3-D simulations. STAR-CD has been widely used mostly for 3-D simulations. To a lesser extent, other commercial software, CFD-ACE+, CFX and PHOENICS, have also been used. In most cases, the SIMPLE (or SIMPLER, SIMPLEC) algorithm is deployed, though in some cases the PISO algorithm is used for its superior coupling quality. One way or the other, the guiding hand of D. Brian Spalding is seen in the development of CFD modeling of PEM fuel cells [144].

5 Summary and Conclusions

PEMFC Modeling approaches have evolved from the early works of Springer and colleagues at Los Alamos National Labs. These treat water transport with the single-phase approach, where water flux is governed by electroosmotic drag and diffusion. Modeling the behavior of the PEMFC with computational fluid dynamics requires understanding of the coupled physics of flow, heat, water, and charge transport in

the MEA and diffusion layers. Different approaches have been used to analyze thermal, water, and charge transport, however, there is some convergence. Several commercially available software packages have incorporated the appropriate physics in add-on modules or subroutines, with flexibility for user modifications.

New developments in in-situ fuel cell experiments, and advanced imaging techniques with in-situ and ex-situ experiments, have enhanced the calibration and validation of the MEA water transport models used in many CFD models. Water management is critical to effective operation of PEMFC. The MEA needs to be hydrated for protonic conductivity, but excessive water produces flooding which blocks supply of reactant gases to reaction sites in the catalyst layers.

There are two main methodological approaches; one- or two-domain. The former meshes and solves the governing differential equations in all parts of the fuel cell, including the electrolyte membrane and catalyst layers, the MEA. Because the catalyst layers are typically 1–2 orders of magnitude thinner than the gas channels, this approach entails adding large numbers of thin, high-aspect ratio cells to the problem, with negative consequences for solution stability and convergence. The other method is the interface approach which does not mesh the MEA, but treats it as an interface which separates the anode and cathode regions. Properties must be prescribed within the interphase, based on empirical relations and analytical solutions, to be used as boundary conditions for the regions. The reliance on experimental data suggests that interface model may need continuous updating as better data become available.

CFD models are now capable of fairly accurate simulation of a single PEMFC in steady or transient operation. Stacks of a few cells can also be simulated with the aid of parallel computing. However, large stacks which contain tens to hundreds of cells are still beyond the resolution ability of most CFD software. These have to be solved in segments, with some clever way devised to patch them together.

References

1. Spalding, D. B. (1951). The combustion of liquid fuels. In *Engineering*. Cambridge, U.K.: Cambridge University Press.
2. Spalding, D. B. (1953). The combustion of liquid fuels. *Symposium (International) on Combustion, 4*(1), 847–864.
3. Spalding, D. B. (1955). Some fundamentals of combustion. In *Gas turbine series* (Vol. 2, 250 pp.). Butterworth's Scientific Publications.
4. Spalding, D. B. (1978). A general theory of turbulent combustion. *Journal of Energy, 2*(1), 16–23.
5. Spalding, D. B. (1979). *Combustion and mass transfer: A textbook with multiple-choice exercises for engineering students* (1st ed., p. vii, 409 pp.). Oxford; New York: Pergamon International Library of Science, Technology, Engineering, and Social Studies, Pergamon Press.
6. Dicks, A., & Rand, D. (2018). *Fuel cell systems explained* (3rd ed.). West Sussex: Wiley.
7. Stone, R. (2003). Competing technologies for transportation. In G. Hoogers (Ed.), *Fuel cell technology handbook*. Boca Raton, FL: CRC Press.
8. Wang, Y., et al. (2011). A review of polymer electrolyte membrane fuel cells: Technology, applications, and needs on fundamental research. *Applied Energy, 88*(4), 981–1007.

9. Dutta, S., Shimpalee, S., & Van Zee, J. W. (2001). Numerical prediction of mass-exchange between cathode and anode channels in a PEM fuel cell. *International Journal of Heat and Mass Transfer, 44,* 2029–2042.
10. Edwards, R. L., & Demuren, A. (2018). Interface model of PEM fuel cell membrane steady-state behavior. *International Journal of Energy and Environmental Engineering*.
11. Wang, C.-Y. (2004). Fundamental models for fuel cell engineering. *Chemical Reviews, 104*(10), 4727–4766.
12. Guvelioglu, G. H., & Stenger, H. G. (2005). Computational fluid dynamics modeling of polymer electrolyte membrane fuel cells. *Journal of Power Sources, 147*(1–2), 95–106.
13. Bednarek, T., & Tsotridis, G. (2017). Issues associated with modelling of proton exchange membrane fuel cell by computational fluid dynamics. *Journal of Power Sources, 343,* 550–563.
14. Hoogers, G. (2003). Fuel cell components and their impact on performance. In G. Hoogers (Ed.), *Fuel cell technology handbook.* Boca Raton, FL: CRC Press.
15. Hoogers, G. (2003). Automotive applications. In G. Hoogers (Ed.), *Fuel cell technology handbook*. Boca Raton, FL: CRC Press.
16. Macedo-Valencia, J., et al. (2016). 3D CFD modeling of a PEM fuel cell stack. *International Journal of Hydrogen Energy, 41*.
17. Siegel, C. (2008). Review of computational heat and mass transfer modeling in polymer-electrolyte-membrane (PEM) fuel cells. *Energy, 33,* 1331–1352.
18. Pharoah, J. G., & Burheim, O. S. (2010). On the temperature distribution in polymer electrolyte fuel cells. *Journal of Power Sources, 195*(16), 5235–5245.
19. Burheim, O., et al. (2010). Ex situ measurements of through-plane thermal conductivities in a polymer electrolyte fuel cell. *Journal of Power Sources, 195*(1), 249–256.
20. Barbir, F. (2013). *PEM fuel cells: Theory and practice*. Academic Press.
21. Wu, H.-W. (2016). A review of recent development: Transport and performance modeling of PEM fuel cells. *Applied Energy, 165,* 81–106.
22. Patankar, S. V., & Spalding, D. B. (1972). A calculation procedure for heat, mass and momentum transfer in three-dimensional parabolic flows. *International Journal of Heat and Mass Transfer, 15,* 1787–1806.
23. Wilberforce, T., et al. (2017). Modelling and simulation of proton exchange membrane fuel cell with serpentine bipolar plate using MATLAB. *International Journal of Hydrogen Energy*.
24. Mench, M. (2008). *Fuel cell engines*. Wiley.
25. Wood, D. L., Yi, J. S., & Nguyen, T. V. (1998). Effect of direct liquid water injection and interdigitated flow field on the performance of proton exchange membrane fuel cells. *Electrochimica Acta, 43*(24), 3795–3809.
26. Laurencelle, F., et al. (2001). Characterization of a Ballard MK5-E proton exchange membrane fuel cell stack. *Fuel Cells, 1*(1), 66–71.
27. Cooper, K. R., et al. (2007). *Experimental methods and data analyses for polymer electrolyte fuel cells*. Scribner Associates, Inc.
28. Ju, H., & Wang, C.-Y. (2004). Experimental validation of a PEM fuel cell model by current distribution data. *Journal of the Electrochemical Society, 151*(11), A1954–A1960.
29. Mench, M. M., Wang, C. Y., & Ishikawa, M. (2003). In situ current distribution measurements in polymer electrolyte fuel cells. *Journal of the Electrochemical Society, 150*(8), A1052–A1059.
30. Wieser, C., Helmbold, A., & Gülzow, E. (2000). A new technique for two-dimensional current distribution measurements in electrochemical cells. *Journal of Applied Electrochemistry, 30*(7), 803–807.
31. Geiger, A. B., et al. (2004). An approach to measuring locally resolved currents in polymer electrolyte fuel cells. *Journal of the Electrochemical Society, 151*(3), A394–A398.
32. Natarajan, D., & Van Nguyen, T. (2005). Current distribution in PEM fuel cells. Part 1: Oxygen and fuel flow rate effects. *AIChE Journal, 51*(9), 2587–2598.
33. Vie, P. J. S., & Kjelstrup, S. (2004). Thermal conductivities from temperature profiles in the polymer electrolyte fuel cell. *Electrochimica Acta, 49*(7), 1069–1077.

34. Mench, M., Burford, D. J., & Davis, T. W. (2003). In situ temperature distribution measurements in an operating polymer electrolyte fuel cell, Paper No. 42393. In *Proceedings of the 2003 International Mechanical Engineering conference and Exposition (IMECE)*. Washington, DC: ASME.
35. Burford, D. J., Davis, T. W., & Mench, M. M. (2004). Heat transport and temperature distribution in PEFCs, IMECEC 2004-59497. In *Proceedings of the 2004 International Mechanical Engineering conference and Exposition (IMECE)*, Anaheim, CA.
36. Mench, M. M., Dong, Q. L., & Wang, C. Y. (2003). In situ water distribution measurements in a polymer electrolyte fuel cell. *Journal of Power Sources, 124*(1), 90–98.
37. Dong, Q., Kull, J., & Mench, M. M. (2005). Real-time water distribution in a polymer electrolyte fuel cell. *Journal of Power Sources, 139*(1–2), 106–114.
38. Edwards, R. L., & Demuren, A. (2016). Regression analysis of PEM fuel cell transient response. *International Journal of Energy and Environmental Engineering, 7*(3), 329–341.
39. Stevens, D. A., & Dahn, J. R. (2003). Electrochemical characterization of the active surface in carbon-supported platinum electrocatalysts for PEM fuel cells. *Journal of the Electrochemical Society, 150*(6), A770–A775.
40. Neyerlin, K. C., et al. (2006). Determination of catalyst unique parameters for the oxygen reduction reaction in a PEMFC. *Journal of the Electrochemical Society, 153*(10), A1955–A1963.
41. Neyerlin, K. C., et al. (2007). Cathode catalyst utilization for the ORR in a PEMFC. *Journal of the Electrochemical Society, 154*(2), B279–B287.
42. Soboleva, T., et al. (2011). PEMFC catalyst layers: The role of micropores and mesopores on water sorption and fuel cell activity. *ACS Applied Materials & Interfaces, 3*(6), 1827–1837.
43. Cooper, K. R., & Smith, M. (2006). Electrical test methods for on-line fuel cell ohmic resistance measurement. *Journal of Power Sources, 160*(2), 1088–1095.
44. Neyerlin, K. C., et al. (2007). Study of the exchange current density for the hydrogen oxidation and evolution reactions. *Journal of the Electrochemical Society, 154*(7), B631–B635.
45. Liu, Y., et al. (2009). Proton conduction and oxygen reduction kinetics in PEM fuel cell cathodes: Effects of ionomer-to-carbon ratio and relative humidity. *Journal of the Electrochemical Society, 156*(8), B970–B980.
46. Kulikovsky, A. A. (2010). Introduction. In A. A. Kulikovsky (Ed.), *Analytical modelling of fuel cells* (pp. xiii–xv). Amsterdam: Elsevier.
47. Uchida, M., et al. (1995). Investigation of the microstructure in the catalyst layer and effects of both perfluorosulfonate ionomer and PTFE-loaded carbon on the catalyst layer of polymer electrolyte fuel cells. *Journal of the Electrochemical Society, 142*(12), 4143–4149.
48. Uchida, M., et al. (1996). Effects of microstructure of carbon support in the catalyst layer on the performance of polymer-electrolyte fuel cells. *Journal of the Electrochemical Society, 143*(7), 2245–2252.
49. Xie, J., et al. (2004). Ionomer segregation in composite MEAs and its effect on polymer electrolyte fuel cell performance. *Journal of the Electrochemical Society, 151*(7), A1084–A1093.
50. Wang, Y., & Feng, X. (2008). Analysis of reaction rates in the cathode electrode of polymer electrolyte fuel cell I. Single-layer electrodes. *Journal of the Electrochemical Society, 155*(12), B1289–B1295.
51. Wang, Y. (2007). Analysis of the key parameters in the cold start of polymer electrolyte fuel cells. *Journal of the Electrochemical Society, 154*(10), B1041–B1048.
52. Stumper, J., Haas, H., & Granados, A. (2005). In situ determination of MEA resistance and electrode diffusivity of a fuel cell. *Journal of the Electrochemical Society, 152*(4), A837–A844.
53. Yu, Z., & Carter, R. N. (2010). Measurement of effective oxygen diffusivity in electrodes for proton exchange membrane fuel cells. *Journal of Power Sources, 195*(4), 1079–1084.
54. Shen, J., et al. (2011). Measurement of effective gas diffusion coefficients of catalyst layers of PEM fuel cells with a Loschmidt diffusion cell. *Journal of Power Sources, 196*(2), 674–678.
55. Yu, Z., Carter, R. N., & Zhang, J. (2012). Measurements of pore size distribution, porosity, effective oxygen diffusivity, and tortuosity of PEM fuel cell electrodes. *Fuel Cells, 12*(4), 557–565.

56. Lange, K. J., Sui, P.-C., & Djilali, N. (2012). Determination of effective transport properties in a PEMFC catalyst layer using different reconstruction algorithms. *Journal of Power Sources, 208,* 354–365.
57. Singh, R., et al. (2014). Dual-beam FIB/SEM characterization, statistical reconstruction, and pore scale modeling of a PEMFC catalyst layer. *Journal of the Electrochemical Society, 161*(4), F415–F424.
58. Durst, J., et al. (2015). Hydrogen oxidation and evolution reaction kinetics on carbon supported Pt, Ir, Rh, and Pd electrocatalysts in acidic media. *Journal of the Electrochemical Society, 162*(1), F190–F203.
59. Gasteiger, H.A., J.E. Panels, and S.G. Yan. (2004). Dependence of PEM fuel cell performance on catalyst loading. *Journal of Power Sources, 127*(1–2), 162–171.
60. Kornyshev, A. A., & Kulikovsky, A. A. (2001). Characteristic length of fuel and oxygen consumption in feed channels of polymer electrolyte fuel cells. *Electrochimica Acta, 46*(28), 4389–4395.
61. Jaouen, F., Lindbergh, G., & Sundholm, G. (2002). Investigation of mass-transport limitations in the solid polymer fuel cell cathode. *Journal of the Electrochemical Society, 149*(4), A437–A447.
62. Neyerlin, K. C., et al. (2005). Effect of relative humidity on oxygen reduction kinetics in a PEMFC. *Journal of the Electrochemical Society, 152*(6), A1073–A1080.
63. Shimpalee, S., et al. (2009). Experimental and numerical studies of portable PEMFC stack. *Electrochimica Acta, 54*(10), 2899–2911.
64. Bernardi, D. M., & Verbrugge, M. W. (1991). Mathematical model of a gas diffusion electrode bonded to a polymer electrolyte. *AIChE Journal, 37*(8), 1151–1163.
65. Springer, T. E., Zawodzinski, T. A., & Gottesfeld, S. (1991). Polymer electrolyte fuel cell model. *Journal of the Electrochemical Society, 138*(8), 2334–2342.
66. Kamarajugadda, S., & Mazumder, S. (2008). On the implementation of membrane models in computational fluid dynamics calculations of polymer electrolyte membrane fuel cells. *Computers & Chemical Engineering, 32*(7), 1650–1660.
67. Zawodzinski, T. A., et al. (1991). Determination of water diffusion coefficients in perfluorosulfonate ionomeric membranes. *The Journal of Physical Chemistry, 95*(15), 6040–6044.
68. Zawodzinski, J. T. A., et al. (1993). Water uptake by and transport through Nafion[sup [registered sign]] 117 membranes. *Journal of the Electrochemical Society, 140*(4), 1041–1047.
69. Hinatsu, J. T., Mizuhata, M., & Takenaka, H. (1994). Water uptake of perfluorosulfonic acid membranes from liquid water and water vapor. *Journal of the Electrochemical Society, 141*(6), 1493–1498.
70. Jalani, N. H., Choi, P., & Datta, R. (2005). TEOM: A novel technique for investigating sorption in proton-exchange membranes. *Journal of Membrane Science, 254*(1–2), 31–38.
71. Onishi, L. M., Prausnitz, J. M., & Newman, J. (2007). Water−Nafion equilibria. Absence of Schroeder's paradox. *The Journal of Physical Chemistry B, 111*(34), 10166–10173.
72. Kusoglu, A., Kienitz, B. L., & Weber, A. Z. (2011). Understanding the effects of compression and constraints on water uptake of fuel-cell membranes. *Journal of the Electrochemical Society, 158*(12), B1504–B1514.
73. Halim, J., et al. (1994). Characterization of perfluorosulfonic acid membranes by conductivity measurements and small-angle X-ray scattering. *Electrochimica Acta, 39*(8–9), 1303–1307.
74. Weber, A. Z., & Newman, J. (2004). Transport in polymer-electrolyte membranes: II. Mathematical model. *Journal of the Electrochemical Society, 151*(2), A311–A325.
75. Motupally, S., Becker, A. J., & Weidner, J. W. (2000). Diffusion of water in Nafion 115 membranes. *Journal of the Electrochemical Society, 147*(9), 3171–3177.
76. Ye, X., & Wang, C.-Y. (2007). Measurement of water transport properties through membrane-electrode assemblies. *Journal of the Electrochemical Society, 154*(7), B676–B682.
77. Ge, S., Yi, B., & Ming, P. (2006). Experimental determination of electro-osmotic drag coefficient in Nafion membrane for fuel cells. *Journal of the Electrochemical Society, 153*(8), A1443–A1450.

78. Büchi, F. N., & Scherer, G. G. (1996). In-situ resistance measurements of Nafion® 117 membranes in polymer electrolyte fuel cells. *Journal of Electroanalytical Chemistry, 404*(1), 37–43.
79. Buchi, F. N., & Scherer, G. G. (2001). Investigation of the transversal water profile in Nafion membranes in polymer electrolyte fuel cells. *Journal of the Electrochemical Society, 148*(Copyright 2001, IEE), 183–188.
80. Kulikovsky, A. A. (2003). Quasi-3D modeling of water transport in polymer electrolyte fuel cells. *Journal of the Electrochemical Society, 150*(11), A1432–A1439.
81. Zhang, Z., et al. (2008). Spatial and temporal mapping of water content across Nafion membranes under wetting and drying conditions. *Journal of Magnetic Resonance, 194*(2), 245–253.
82. Gebel, G., et al. (2011). The kinetics of water sorption in Nafion membranes: A small-angle neutron scattering study. *Journal of Physics: Condensed Matter, 23*(23), 234107.
83. Tabuchi, Y., et al. (2011). Analysis of in situ water transport in Nafion® by confocal micro-Raman spectroscopy. *Journal of Power Sources, 196*(2), 652–658.
84. Hara, M., et al. (2011). Temperature dependence of the water distribution inside a Nafion membrane in an operating polymer electrolyte fuel cell. A micro-Raman study. *Electrochimica Acta, 58,* 449–455.
85. Hwang, G. S., et al. (2013). Understanding water uptake and transport in Nafion using X-ray microtomography. *ACS Macro Letters, 2*(4), 288–291.
86. Tsushima, S., Teranishi, K., & Hirai, S. (2004). Magnetic resonance imaging of the water distribution within a polymer electrolyte membrane in fuel cells. *Electrochemical and Solid-State Letters, 7*(9), A269–A272.
87. Tsushima, S., et al. (2010). Investigation of water distribution in a membrane in an operating PEMFC by environmental MRI. *Journal of the Electrochemical Society, 157*(12), B1814–B1818.
88. Chen, F., et al. (2004). Transient behavior of water transport in the membrane of a PEM fuel cell. *Journal of Electroanalytical Chemistry, 566*(1), 85–93.
89. Berg, P., et al. (2004). Water management in PEM fuel cells. *Journal of the Electrochemical Society, 151*(3), A341–A353.
90. Majsztrik, P. W., et al. (2007). Water sorption, desorption and transport in Nafion membranes. *Journal of Membrane Science, 301*(1–2), 93–106.
91. Monroe, C. W., et al. (2008). A vaporization-exchange model for water sorption and flux in Nafion. *Journal of Membrane Science, 324*(1–2), 1–6.
92. Ge, S., et al. (2005). Absorption, desorption, and transport of water in polymer electrolyte membranes for fuel cells. *Journal of the Electrochemical Society, 152*(6), A1149–A1157.
93. Adachi, M. (2010). *Proton exchange membrane fuel cells: Water permeation through Nafion (R) membranes*. Department of Chemistry-Simon Fraser University.
94. Adachi, M., et al. (2010). Thickness dependence of water permeation through proton exchange membranes. *Journal of Membrane Science, 364*(1–2), 183–193.
95. Adachi, M., et al. (2010). Water permeation through catalyst-coated membranes. *Electrochemical and Solid-State Letters, 13*(6), B51–B54.
96. Meng, H., & Wang, C.-Y. (2004). Electron transport in PEFCs. *Journal of the Electrochemical Society, 151*(3), A358–A367.
97. Meng, H., & Wang, C. Y. (2005). Multidimensional modelling of polymer electrolyte fuel cells under a current density boundary condition. *Fuel Cells, 5*(4), 455–462.
98. Khandelwal, M., & Mench, M. M. (2006). Direct measurement of through-plane thermal conductivity and contact resistance in fuel cell materials. *Journal of Power Sources, 161*(2), 1106–1115.
99. Ramousse, J., et al. (2008). Estimation of the effective thermal conductivity of carbon felts used as PEMFC gas diffusion layers. *International Journal of Thermal Sciences, 47*(1), 1–6.
100. Sadeghi, E., Djilali, N., & Bahrami, M. (2011). Effective thermal conductivity and thermal contact resistance of gas diffusion layers in proton exchange membrane fuel cells. Part 1: Effect of compressive load. *Journal of Power Sources, 196*(1), 246–254.

101. Teertstra, P., Karimi, G., & Li, X. (2011). Measurement of in-plane effective thermal conductivity in PEM fuel cell diffusion media. *Electrochimica Acta, 56*(3), 1670–1675.
102. Ji, M., & Wei, Z. (2009). A review of water management in polymer electrolyte membrane fuel cells. *Energies, 2*(4), 1057–1106.
103. Bernardi, D. M., & Verbrugge, M. (1992). A mathematical model of the solid polymer electrolyte fuel cell. *Journal of the Electrochemical Society, 139.*
104. Baschuk, J. J., & Li, X. (2000). Modelling of polymer electrolyte membrane fuel cells with variable degrees of water flooding. *Journal of Power Sources, 86*(1), 181–196.
105. Djilali, N., & Lu, D. (2002). Influence of heat transfer on gas and water transport in fuel cells. *International Journal of Thermal Sciences, 41*(1), 29–40.
106. Yan, W.-M., et al. (2004). *Analysis of thermal and water management with temperature-dependent diffusion effects in membrane of proton exchange membrane fuel cells* (Vol. 129, pp. 127–137).
107. Song, D., et al. (2006). Transient analysis for the cathode gas diffusion layer of PEM fuel cells. *Journal of Power Sources, 159*(2), 928–942.
108. Falcão, D. S., et al. (2011). 1D and 3D numerical simulations in PEM fuel cells. *International Journal of Hydrogen Energy, 36.*
109. Gurau, V., Liu, H., & Kakaç, S. (1998). Two-dimensional model for proton exchange membrane fuel cells. *AIChE Journal, 44*(11), 2410–2422.
110. Yi, J., & Nguyen, T. (1998). An along-the-channel model for proton exchange membrane fuel cells. *Journal of the Electrochemical Society, 145,* 1149–1159.
111. Um, S., Wang, C. Y., & Chen, K. S. (2000). Computational fluid dynamics modeling of proton exchange membrane fuel cells. *Journal of the Electrochemical Society, 147*(12), 4485–4493.
112. Siegel, N., et al. (2003). Single domain PEMFC model based on agglomerate catalyst geometry. *Journal of Power Sources, 115,* 81–89.
113. Siegel, N., et al. (2004). A two-dimensional computational model of a PEMFC with liquid water transport. *Journal of Power Sources, 128,* 173–184.
114. Grujicic, M., & Chittajallu, K. M. (2004). Design and optimization of polymer electrolyte membrane (PEM) fuel cells. *Applied Surface Science, 227*(1–4), 56–72.
115. Sui, P. C., & Djilali, N. (2006). Analysis of coupled electron and mass transport in the gas diffusion layer of a PEM fuel cell. *Journal of Power Sources, 161*(1), 294–300.
116. Seddiq, M., Khaleghi, H., & Mirzaei, M. (2006). Numerical analysis of gas cross-over through the membrane in a proton exchange membrane fuel cell. *Journal of Power Sources, 161*(1), 371–379.
117. Lin, H.-H., et al. (2006). Optimization of key parameters in the proton exchange membrane fuel cell. *Journal of Power Sources, 162,* 246–254.
118. Meng, H. (2007). Numerical investigation of transient responses of a PEM fuel cell using a two-phase non-isothermal mixed-domain model. *Journal of Power Sources, 171*(2), 738–746.
119. Beale, S., et al. (2009). Two-phase flow and mass transfer within the diffusion layer of a polymer electrolyte membrane fuel cell. *Computational Thermal Sciences, 1.*
120. Spalding, D. B. (1984). *PHOENICS 84: A multi-dimensional multi-phase general-purpose computer simulator for fluid flow, heat transfer and combustion: 36 lecture panels.*
121. Spalding, D. B. (1981). Numerical computation of multiphase fluid flow and heat transfer. In C. Taylor & K. Morgan (Eds.), *Recent advances in numerical methods in fluids* (pp. 161–191). Swansea: Pineridge Press.
122. Pourmahmoud, N., et al. (2011). Three-dimensional numerical analysis of proton exchange membrane fuel cell. *Journal of Mechanical Science and Technology, 25*(10), 2665–2673.
123. Meng, H., & Wang, C.-Y. (2004). Large-scale simulation of polymer electrolyte fuel cells by parallel computing. *Chemical Engineering Science, 59*(16), 3331–3343.
124. Wu, H., Li, X., & Berg, P. (2009). On the modeling of water transport in polymer electrolyte membrane fuel cells. *Electrochimica Acta, 54*(27), 6913–6927.
125. Chiu, H.-C., et al. (2012). A three-dimensional modeling of transport phenomena of proton exchange membrane fuel cells with various flow fields. *Applied Energy, 96,* 359–370.

126. Zhou, T., & Liu, H. T. (2001). A general three-dimensional model for proton exchange membrane fuel cells. *International Journal of Transport Phenomena, 3,* 177–198.
127. You, L., & Liu, H. (2002). A two-phase flow and transport model for the cathode of PEM fuel cells. *International Journal of Heat and Mass Transfer, 45*(11), 2277–2287.
128. You, L., & Liu, H. (2001). A parametric study of the cathode catalyst layer of PEM fuel cells using a pseudo-homogeneous model. *International Journal of Hydrogen Energy, 26*(9), 991–999.
129. Dutta, S., Shimpalee, S., & Van Zee, J. W. (2000). Three-dimensional numerical simulation of straight channel PEM fuel cells. *Journal of Applied Electrochemistry, 30,* 135–146.
130. Shimpalee, S., & Dutta, S. (2000). Numerical prediction of temperature distribution in PEM fuel cells. *Numerical Heat Transfer, Part A: Applications, 38*(2), 111–128.
131. Sui, P. C., & Djilali, N. (2005). Analysis of water transport in proton exchange membranes using a phenomenological model. *Journal of Fuel Cell Science and Technology, 2*(3), 149–155.
132. Mazumder, S. (2005). A generalized phenomenological model and database for the transport of water and current in polymer electrolyte membranes. *Journal of the Electrochemical Society, 152*(8), A1633–A1644.
133. Um, S., & Wang, C. Y. (2000). Three dimensional analysis of transport and reaction in PEMFC. In *ASME fuel cell division* (pp. 19–25). ASME: Orlando, FL.
134. Um, S., & Wang, C. Y. (2004). Three-dimensional analysis of transport and electrochemical reactions in polymer electrolyte fuel cells. *Journal of Power Sources, 125*(1), 40–51.
135. Wang, Y., & Wang, C.-Y. (2005). Modeling polymer electrolyte fuel cells with large density and velocity changes. *Journal of the Electrochemical Society, 152*(2), A445–A453.
136. Carnes, B., et al. (2013). Validation of a two-phase multidimensional polymer electrolyte membrane fuel cell computational model using current distribution measurements. *Journal of Power Sources, 236,* 126–137.
137. Bvumbe Tatenda, J., et al. (2016). Review on management, mechanisms and modelling of thermal processes in PEMFC. *Hydrogen and Fuel Cells, 1*(1), 1–20.
138. Berning, T., Lu, D. M., & Djilali, N. (2002). Three-dimensional computational analysis of transport phenomena in a PEM fuel cell. *Journal of Power Sources, 106*(1–2), 284–294.
139. Mazumder, S., & Cole, J. V. (2003). Rigorous 3-D mathematical modeling of PEM fuel cells. *Journal of the Electrochemical Society, 150*(11), A1503–A1509.
140. Mazumder, S., & Cole, J. V. (2003). Rigorous 3-D mathematical modeling of PEM fuel cells. *Journal of the Electrochemical Society, 150*(11), A1510–A1517.
141. Al-Baghdadi, M. A. R. S. (2008). *CFD models for analysis and design of PEM fuel cells*. New York: Nova Science Publishers.
142. Schwarz, D. H., & Beale, S. B. (2009). Calculations of transport phenomena and reaction distribution in a polymer electrolyte membrane fuel cell. *International Journal of Heat and Mass Transfer, 52*(17–18), 4074–4081.
143. Strahl, S., Husar, A., & Franco, A. A. (2014). Electrode structure effects on the performance of open-cathode proton exchange membrane fuel cells: A multiscale modeling approach. *International Journal of Hydrogen Energy, 39*(18), 9752–9767.
144. Artemov, V., et al. (2009). A tribute to D. B. Spalding and his contributions in science and engineering. *International Journal of Heat and Mass Transfer, 52,* 3884–3905.